Monthly Notices
of the
ROYAL ASTRONOMICAL SOCIETY

MNRAS **541,** 2134–2161 (2025) https://doi.org/10.1093/mnras/staf1083
Advance Access publication 2025 July 3

JADES – the small blue bump in GN-z11: insights into the nuclear region of a galaxy at $z = 10.6$

Xihan Ji [1,2]★ Roberto Maiolino,[1,2,3] Gary Ferland,[4] Francesco D'Eugenio [1,2]
Rachana Bhatawdekar [5] Stéphane Charlot [6] Jacopo Chevallard [7] Mirko Curti,[8]
Emma Curtis-Lake [9] Kevin Hainline,[10] Zhiyuan Ji,[10] Brant Robertson,[11] Bruno Rodríguez Del Pino,[12]
Jan Scholtz [1,2] Sandro Tacchella [1,2] Christina C. Williams[13] and Joris Witstok [1,2,14,15]

[1] *Kavli Institute for Cosmology, University of Cambridge, Madingley Road, Cambridge CB3 0HA, UK*
[2] *Cavendish Laboratory, University of Cambridge, 19 JJ Thomson Avenue, Cambridge CB3 0HE, UK*
[3] *Department of Physics and Astronomy, University College London, Gower Street, London WC1E 6BT, UK*
[4] *Department of Physics and Astronomy, University of Kentucky, 505 Rose Street, Lexington, KY 40506, USA*
[5] *European Space Agency (ESA), European Space Astronomy Centre (ESAC), Camino Bajo del Castillo s/n, E-28692 Villanueva de la Cañada, Madrid, Spain*
[6] *CNRS, UMR 7095, Institut d'Astrophysique de Paris, Sorbonne Université, 98 bis bd Arago, F-75014 Paris, France*
[7] *Department of Physics, University of Oxford, Denys Wilkinson Building, Keble Road, Oxford OX1 3RH, UK*
[8] *European Southern Observatory, Karl-Schwarzschild-Strasse 2, D-85748 Garching, Germany*
[9] *Centre for Astrophysics Research, Department of Physics, Astronomy and Mathematics, University of Hertfordshire, Hatfield AL10 9AB, UK*
[10] *Steward Observatory, University of Arizona, 933 N. Cherry Avenue, Tucson, AZ 85721, USA*
[11] *Department of Astronomy and Astrophysics University of California, Santa Cruz, 1156 High Street, Santa Cruz CA 96054, USA*
[12] *Centro de Astrobiología (CAB), CSIC–INTA, Cra. de Ajalvir Km. 4, E-28850 - Torrejón de Ardoz, Madrid, Spain*
[13] *NSF's National Optical-Infrared Astronomy Research Laboratory, 950 North Cherry Avenue, Tucson, AZ 85719, USA*
[14] *Cosmic Dawn Center (DAWN), Elektrovej 327, 2800 Kgs. Lyngby, Copenhagen, Denmark*
[15] *Niels Bohr Institute, University of Copenhagen, Jagtvej 128, DK-2200 Copenhagen, Denmark*

Accepted 2025 June 30. Received 2025 June 20; in original form 2024 May 9

ABSTRACT

We report the detection of continuum excess in the rest-frame ultraviolet (UV) between 3000 and 3550 Å in the *JWST*/Near Infrared Spectrograph (NIRSpec) spectrum of GN-z11, a luminous galaxy $z = 10.603$. The shape of the continuum excess resembles a Balmer continuum, but has a break around 3546 Å. The fitting result of this excess depends on the assumed origin of the continuum. If the continuum of GN-z11 is dominated by a stellar population with a small Balmer break, the apparent blueshift of the Balmer continuum is not significant and the best-fitting Balmer continuum model indicates a temperature of $T_e = 1.78^{+0.25}_{-0.21} \times 10^4$ K. In contrast, if the continuum is dominated by active galactic nucleus emission, a nebular continuum model cannot fit the spectrum properly. The absence of the Balmer jump indicates an electron temperature of $\sim 3 \times 10^4$ K, significantly higher than the temperature of $T_e(\mathrm{O}^{2+}) = 1.36 \pm 0.13 \times 10^4$ K inferred from [O III]λ4363 and [O III]λ5007. The temperature difference can result from mixing of different ionized regions: the Balmer emission mainly arises from dense and hot clouds in the broad-line region, whereas the forbidden lines originate from less dense and colder gas. An alternative explanation for the observed continuum excess is the Fe II emission, which shows a characteristic jump blueward of the Balmer limit as previously seen in the spectra of many lower redshift quasars. Through comparisons with CLOUDY models, we show an Fe abundance above $\sim 1/3$ solar is likely needed, which could be achieved via enrichment from Type-Ia supernovae, hypernovae, or pair-instability supernovae.

Key words: galaxies: abundances – galaxies: active – galaxies: evolution – galaxies: high-redshift.

1 INTRODUCTION

The ulraviolet (UV) spectra of Type-1 active galactic nuclei (AGNs) often show prominent continuum excess extending from 2000 to 4000 Å, which is also known as the '3000 Å excess' or the 'small blue bump' (Neugebauer et al. 1979; Richstone & Schmidt 1980; Grandi 1982). Early observations show the small blue bumps in quasars exhibit a variety of shapes and are found to show variability weakly correlated with that of the UV continuum (e.g. Ulrich et al. 1980; Ulrich, Maraschi & Urry 1997). In addition, polarization analyses of the spectrum of the Seyfert-1 galaxy NGC 4151 show the small blue bump has a similar polarization as that of broad emission lines, implying a photoionization origin in the broad-line region (BLR; Schmidt & Miller 1980).

★ E-mail: xj274@cam.ac.uk

The commonly adopted explanation for the UV continuum excess is a combination of Fe II emission and Balmer continuum (e.g. Grandi 1981, 1982; Malkan & Sargent 1982; Wills, Netzer & Wills 1985; Dietrich et al. 2003; Kovačević, Popović & Kollatschny 2014). In BLRs, collisional excitation of Fe$^+$, fluorescence by Fe II lines as well other emission lines with similar wavelengths, and radiative excitation by the AGN continuum are able to produce strong Fe II emission (Netzer & Wills 1983; Wills et al. 1985; Penston 1987). Another important factor that enables detectable Fe II emission in BLRs is the sublimation of dust grains, as Fe is usually significantly depleted onto dust in the interstellar medium (ISM; Jenkins 2009). However, it is also suggested that the varying strength of Fe II in observations might indicate the occasional overlap of the Fe II-emitting region with regions outside the dust sublimation radius (Shields, Ludwig & Salviander 2010). Due to the dense energy levels of Fe$^+$ and fast motions of clouds within BLRs, Fe II emission lines are usually highly blended in observations and form a pseudo-continuum spanning from the rest-frame UV to optical. Still, in both observations and theoretical models of the Fe II pseudo-continuum, the Fe II emission can be divided by groups of broad emission centring at different wavelengths, whose relative strengths are determined by a series parameters including the optical depth, the velocity of microturbulence, the metallicity, and so forth (e.g. Baldwin et al. 2004; Ferland et al. 2009; Sarkar et al. 2021). The edges of the Fe II groups, especially between the UV and optical groups, are prominent in some quasar spectra and resemble sharp jumps in the pseudo-continuum excess (e.g. Tsuzuki et al. 2006).

Besides the Fe II emission, a Balmer continuum is often needed for a complete fit of the UV spectra of Type-1 AGNs. The Balmer continuum contributes to a smoothly rising component of the continuum until the Balmer limit at 3646 Å. The Balmer continuum is produced by the recombination of free electrons to the $n = 2$ level of hydrogen. The presence of the Balmer continuum provides an independent probe of the gas temperature. This is because the ratio between the intensity of the Balmer continuum at the Balmer limit and that of any given Balmer line decreases with increasing temperature roughly following a power-law relation (Peimbert 1967). As temperature increases, while the whole nebular continuum becomes stronger, the relative strength of the Balmer jump becomes weaker with respect to the intensity of Balmer lines. According to the widely adopted BLR model with a stratified ionization structure, H I emission including the Balmer continuum comes from clouds closer to the accretion disc compared to Fe II emission, leading to the stronger variability of H I emission in observations (Ulrich et al. 1997). The Balmer continuum is also visible in nearby H II regions and planetary nebulae (PNe; Peimbert, Peimbert & Delgado-Inglada 2017) and has been used as an independent temperature probe (e.g. Liu et al. 2001). At high redshift, as revealed recently by *JWST* observations, strong Balmer continua were reported in several systems from either AGN or young stellar populations (e.g. Cameron et al. 2024; Ji et al. 2024; Katz et al. 2024; Tacchella et al. 2025).

On one hand, for AGNs, understanding the origin of the small blue bump and decomposing the contributions from different nebular emissions are important for constraining the Fe abundance as well as the electron temperature of the BLR. While the flux ratio of Mg II$\lambda\lambda$2796, 2803/Fe II measured in the rest-frame UV has been used as an empirical proxy of the abundance ratio of α/Fe in Type-1 AGNs, the accurate determination of the Fe abundance requires detailed modelling of the physical conditions within BLRs (Maiolino & Mannucci 2019). Previous theoretical modelling attempts have shown it is particularly challenging to reproduce the various strengths of the observed Fe II complex (Gaskell et al. 2022). Although significant progress has been made by implementing complex energy levels of Fe$^+$ as well as physical processes such as self-fluorescence and continuum pumping in photoionization simulations, the current application of the theoretical approach is limited to a few well-observed sources and certain parameter regimes (e.g. I Zwicky 1; Sarkar et al. 2021). As the UV spectrum becomes increasingly important for spectroscopic studies of AGNs in the early Universe, it is vital to understand the UV signatures of AGNs over a broader parameter space. On the other hand, for both AGNs and star-forming (SF) galaxies, independent temperature determinations from the Balmer jump can provide important clues on the temperature structures and chemical abundance patterns. The main limiting factor for constraining the Balmer temperature in BLRs, however, is the degeneracy between the strength of the Balmer continuum and that of the Fe II complex.

With the advent of the *JWST* (Gardner et al. 2023; Rigby et al. 2023), a diverse population of AGNs has been revealed at $z \sim 2 - 11$ (Kocevski et al. 2023; Onoue et al. 2023; Übler et al. 2023, 2024; Furtak et al. 2024; Greene et al. 2024; Matthee et al. 2024; Maiolino et al. 2024a, c; Scholtz et al. 2025). Meanwhile, emission-line studies based on *JWST*/Near-Infrared Spectrograph (NIRSpec, Jakobsen et al. 2022) have shown the prevalence of highly ionized and metal-poor gas in the early Universe (e.g. Curti et al. 2023, 2024; Sanders et al. 2023, 2024; Tacchella et al. 2023a; Cameron et al. 2023b; Laseter et al. 2024). At this parameter regime, the behaviour of the small blue bump remains unexplored. A naive expectation might be that the small blue bump becomes less important and even vanishes in the BLRs of very early AGNs because of low Fe abundances and high electron temperatures. However, in this manuscript, we report the discovery of a significantly detected UV continuum excess in the *JWST*/NIRSpec spectrum of GN-z11, a luminous galaxy at $z = 10.603$ (Oesch et al. 2016; Bunker et al. 2023; Tacchella et al. 2023b; Maiolino et al. 2024a), which partly resembles the shape of the small blue bumps previously observed in lower redshift AGNs.

Notably, the *JWST* observations of the UV nebular emission of GN-z11 can be well explained by ionization of an accreting black hole according to the recent works by Scholtz et al. (2024) and Maiolino et al. (2024a, b). A careful analysis on the multiplet ratios of N III]λ1746 − 1754 and the doublet ratio of N IV]$\lambda\lambda$1483, 1486 measured from the medium-resolution NIRSpec spectrum of GN-z11 indicates a high electron density of $n_e \gtrsim 10^9$ cm^{-3}, typical of the physical conditions in BLRs, while unseen in the ISM (Maiolino et al. 2024a). The AGN identification is further supported by the detection of transitions typical of AGN, such as the C II*1335 fluorescent emission and [Ne IV]λ2424, high-velocity ionized winds seen in C IV$\lambda\lambda$1548, 1550 (Maiolino et al. 2024a), ionization cones in C III]$\lambda\lambda$1906, 1908 (Maiolino et al. 2024b), and an extended Lyα halo, whose brightness and extent is consistent with what observed in quasars at $z \sim 6$ and inconsistent with typical SF galaxies at similar redshifts (Scholtz et al. 2024). The measured widths of permitted lines in GN-z11 from NIRSpec median-resolution spectra are narrower than those typically found in lower-z Type-1 AGNs (Maiolino et al. 2024a), but in the range of those seen in the so-called narrow-line Seyfert 1s (NLSy1s; Osterbrock & Pogge 1985; Goodrich 1989; Leighly 1999), and compatible with a low-mass black hole with $M_{\rm BH} \sim 1.6 \times 10^6$ M$_\odot$. Meanwhile, Maiolino et al. (2024a) estimated an Eddington ratio of 5 (with an uncertainty of a factor of 2), further showing that GN-z11 is similar to NLSy1s, which are usually highly accreting systems. It is worth noticing, in the context of this paper, that NLSy1s tend to show prominent Fe II emissions (e.g. Véron-Cetty, Véron & Gonçalves 2001; Vestergaard & Wilkes 2001; Komossa 2008). Interestingly, the existence of strong nitrogen lines suggests a supersolar N/O ∼ 430 Myr after the big bang, indicative of either an exotic chemical enrichment history in this galaxy or a past chemical enrichment within the small BLR (Bunker et al. 2023; Cameron et al. 2023a; Senchyna et al. 2024; Maiolino et al. 2024a). Since the first Type-Ia supernovae (SNe) that are capable of enriching Fe can occur as early as ∼ 30 Myr after the initial star formation (e.g. Maiolino & Mannucci 2019), if there has been past chemical enrichment in the BLR, one might expect Fe has also been enriched by a few SNe given the likely active star formation in GN-z11 over the past 20–50 Myr (Tacchella et al. 2023b).

We also note that some other works argue young stellar populations from a recent starburst might instead dominate the light of GN-z11 (e.g. Bunker et al. 2023; Charbonnel et al. 2023; Cameron et al. 2023a; Senchyna et al. 2024; Álvarez-Márquez et al. 2025). For example, Bunker et al. (2023) show that the UV line ratios of GN-z11 lie in the transition zone between AGN and SF models of Feltre, Charlot & Gutkin (2016) and Gutkin, Charlot & Bruzual (2016) in the UV diagnostic diagram proposed by Nakajima et al. (2018), although we caution that the possibility of a super-Eddington accreting black hole in GN-z11 might lead to softer ionizing radiation compared to typical AGNs (e.g. Lambrides et al. 2024). Also, it remains unclear whether the UV lines contain a broad component. More recently, Álvarez-Márquez et al. (2025) reported non-detection of any broad component in Hα using the *JWST*/mid-infrared instrument (MIRI) medium-resolution spectroscopy (MRS) observations of GN-z11. Still, Álvarez-Márquez et al. (2025) claimed an underlying broad component in Hα is not ruled out due to the limited signal-to-noise ratio (S/N). In fact, according to Álvarez-Márquez et al. (2025), the broad Hα associated with AGN identified in Maiolino et al. (2024a) would not be detectable in their MIRI spectrum and, therefore, it is plausible that the AGN light is more dominant in the rest-frame UV.

Regardless of the dominant ionizing source in GN-z11, the existence of a 'small blue bump' at $z = 10.603$ raises questions about whether the chemical enrichment processes and temperature structures in early galaxies and/or AGNs differ from those at later cosmic epochs. We show that such a bump is potentially inconsistent with being associated with a Balmer jump; this implies that the temperature associated with the Balmer lines must be much higher than that inferred from the auroral (forbidden) transition, [O III]λ4363, further confirming that the Balmer lines predominantly come from the BLR. We then interpret the small bump similarly as in other Type-1 AGNs (i.e. associated with the Fe complex, although likely with different properties relative to local AGN).

The layout of the manuscript is as follows. In Sections 2 and 3, we describe the observational data we use as well as the spectral measurements. In Section 4, we introduce our method to analyse the observed continuum. In Sections 5 and 6, we compare the observed UV continuum excess with nebular emission models as well as previously observed broad-line AGN spectra to identify potential contributions from the Balmer continuum, Fe II emission, and other nebular emission. We discuss the physical interpretations for the shape and variation of the UV continuum excess as well as the temperature structures in the ionized clouds in Section 7. We also comment on potential emission from other atoms and ions in this wavelength regime. In Section 8, we present our conclusions and outlooks.

2 OBSERVATIONS AND DATA REDUCTION

In this work, we use observational data obtained by *JWST*/NIRSpec. We focus on the low-resolution Prism/CLEAR observations of GN-z11 that cover the rest-frame UV-to-optical regime. Our sample galaxy, GN-z11, was originally detected by the *Hubble Space Telescope* (*HST*) in the Cosmic Assembly Near-infrared Deep Extragalactic Legacy Survey (CANDELS) Great Observatories Origins Deep Survey (GOODS) North field (Grogin et al. 2011; Koekemoer et al. 2011; Oesch et al. 2016) and was later observed in the JWST Advanced Deep Extragalactic Survey (JADES) under the Cycle 2 Program ID 1181 (PI.: D. Eisenstein; Eisenstein et al. 2023a). The spectrum was obtained by combining observations from two different epochs and the detailed descriptions of the observations and data reduction are given by Bunker et al. (2023) and Maiolino et al. (2024a). In brief, there are two sets of observations obtained in 2023 February and May, respectively. The February observation consists of four NIRSpec microshutter assembly (MSA; Ferruit et al. 2022; Jakobsen et al. 2022; Böker et al. 2023) configurations, with 14 groups per integration, one integration per exposure, and three nods each. Each configuration was repeated two times, for a total of 6.9 h exposure time. The May observation consists of three MSA configurations, again with 14 groups per integration, one integration per exposure and three nods, but each configuration was used only one time, for a total of 2.6 h exposure time. The basic information of the two observations is summarized in Table 1.

Table 1. Summary of GN-z11 observations used in this work.

NIRSpec ID —	Date —	PA[a] (deg)	Exp. time (h)	δx[b] (arcsec)	δy (arcsec)
3991	07-Feb-2023	19.57	6.9	0.025	0.021
5591	05-May-2023	289.05	2.6	0.002	0.041

Notes. [a] NIRSpec position angle. [b] In the MSA reference, with x increasing from Q1 to Q3 and y increasing from Q1 to Q2 (Ferruit et al. 2022). The uncertainties on these values is due to a combination of uncertainties in the source position, astrometry, and the precision of the target acquisition (in both observations, the maximum allowed of eight target acquisition sources was used).

The reduction of these observations were carried out using the JADES data reduction pipeline (DRP, D'Eugenio et al. 2025), which is the same as the one described in Curtis-Lake et al. (2023), Curti et al. (2024), and Bunker et al. (2024). The initial processing of the raw data frames used the Space Telescope Science Institute (STScI) pipeline (version 1.16.1, reference file `jwst_1303.pmap`). At this stage, we remove the detector bias and dark current, identify snowballs, and convert the multiple reads to count rates. As part of this latter step, saturation and jumps due to cosmic rays are identified and removed. At this stage, we continue the reduction using a custom pipeline developed by the ESA NIRSpec Science Operations Team, whose essential steps are described in Alves de Oliveira et al. (2018) and Ferruit et al. (2022). A full description will be presented in Carniani et al. (in preparation). The background is removed in the 2D detector images, by subtracting from each shutter the average of the other two shutters, exploiting the 3-nod observing pattern. This procedure takes into account the presence of neighbours/interlopers and of disobedient shutters. After this step, we possess a set of 2D spectra, which are individually flat-fielded and corrected for wavelength-dependent losses due to the telescope and instrument optics. The 2D spectra are then flux calibrated using the static calibration files, which take into account optical distortions. The individual 2D spectra are also corrected for position-dependent slit losses, assuming a point-source geometry. This latter step is not entirely appropriate for GN-z11, given the presence of an extended component (half-light radius 0.05 arcsec) in addition to the point source (Tacchella et al. 2023b). Yet the point-source contribution is dominant (0.6 mag brighter), and does display an flux excess at 4 μm (unlike the extended component; Tacchella et al. 2023b, their fig. 6). To take into account the uncertain position of the source inside the microshutter (due to a combination of uncertainties in the source centre, in the relative astrometry, and in the target acquisition), we tested the effect of random offsets in the nominal source position, drawing from a uniform distribution with width 0.05 arcsec; these changes have negligible effect on localized spectral features (Baker et al., in preparation). After the path-loss corrections are applied, the 2D spectra are rectified. To avoid excessive correlation, we Nyquist sample the instrument line spread function (LSF; Jakobsen et al. 2022), which results in a non-monotonic wavelength grid, with the widest spectral pixels around $\lambda = 1.5$ μm, where the spectral resolution reaches its minimum. The procedure takes into account the nominal intra-shutter position (Table 1) of each observation for the effect of slit underfilling (Ferruit et al. 2022) on the wavelength calibration. We note that our correction still leaves wavelength offsets at the level of 0.1 pixel (D'Eugenio et al. 2025), but these can only be identified statistically using a large sample, and their subpixel magnitude means that they are unlikely to change our results. Uncertainties on the surface brightness (and data-quality flags) are propagated at each step; we use the variance-conserving resampling (Dorner et al. 2016) to take into account correlated noise between adjacent spectral pixels due to the finite spectral resolution.[1] By comparing the pipeline noise to the local standard deviation of the data (after taking into account spectral variations such as the spectral slope and emission lines), we find that the pipeline noise is typically 15 per cent larger than the local standard deviation; this is expected, given that the latter does not account for correlated noise, which reduces the standard deviation of any local sample. For a direct estimate of the covariance matrix between spectral pixels see Witstok et al. (2025) and Jakobsen et al. (in preparation). The 1D spectrum is obtained by extracting from each of the 2D spectra using a 5-pixel box-car extraction, and then combining the resulting 1D spectra using inverse variance weighting and 5σ clipping. Note that inverse-variance weighting does not conserve the flux for features dominated by shot noise. However, GN-z11 like most high-redshift sources is dominated by detector noise, so this issue is not a concern.

3 SPECTRAL MEASUREMENTS

Fig. 1 shows the 1D NIRSpec/Prism spectrum of GN-z11, where we marked locations of prominent emission lines. We measured the fluxes of important emission lines including Hγ, Hδ, [O III]λ4363, [Ne III]λ3869, and [O II]$\lambda\lambda$3726, 3729 in the Prism spectrum for the derivation of the electron temperature and oxygen abundance. To measure the emission lines, we used the the penalized pixel-fitting code (PPXF; Cappellari & Emsellem 2004; Cappellari 2017) and fitting emission lines as Gaussians convolved with the LSFs for point sources observed by MSA Prism given by de Graaff et al. (2024). We limited our fit to the spectral regime of 1350–4550 Å in the rest frame (1.57–5.68 μm in the observed frame) to avoid the region near the Lyα damping wing. During the fit, we tied the kinematics of Balmer lines and forbidden lines separately to account for their potentially different origins in the galaxy. For the continuum, we approximate it as a piecewise power law with break locations at $\lambda = 3000$ and 3550 Å multiplied by a fourth-order polynomial. The first break location is to describe the change in the slope shown in Fig. 1, and the second break location is to describe the jump in the spectrum also shown in Fig. 1. We also tried setting the second break location at the Balmer limit of $\lambda = 3646$ Å, which does not change the line fluxes significantly but results in a larger reduced χ^2. The choice of the flexible modelling for the continuum is to measure the line fluxes without assuming any physical origin for the continuum. The physically motivated fits for the continuum are discussed in Sections 5 and 6. To estimate the flux uncertainties, we manually added noise to the original spectrum. For each pixel, we drew the corresponding noise from a Gaussian distribution with a mean of zero and a standard deviation that equals to the uncertainty of the flux density reported by the DRP. We then fitted the spectrum with PPXF to obtain line fluxes. The above procedure was repeated 500 times and for each emission line, we took the 68 per cent confidence interval of the flux distribution and divided it by $2\sqrt{2}$ to obtain the final uncertainty estimate.[2] While PPXF provides formal errors for line fluxes propagated from the input flux density uncertainties, these uncertainties are computed through the logarithmically rebinned spectrum in the wavelength space (Cappellari 2017) and the bootstrapping method we adopted is generally more robust for estimating uncertainties. We summarize the fluxes of major emission lines in Table 2 and spectral fitting results in Fig. 2. We emphasize that the continuum model we adopted here has no physical meaning and is only used as a smooth baseline for extracting emission-line fluxes. We compared our flux measurements with those by Bunker et al. (2023) and Maiolino et al. (2024a) and confirmed good consistency. Later in our analyses, we also combine the recent *JWST*/MIRI MRS measurement of the optical [O III]λ5007 flux of GN-z11 reported in Álvarez-Márquez et al. (2025), which is $1.36 \pm 0.14 \times 10^{-17}$ erg s^{-1} cm^{-2}.

Besides the prominent emission lines mentioned above, the spectrum of GN-z11 shows a clear excess above the simple power-law continuum, roughly between 3000 and 3550 Å in the rest frame. We marked the region showing the continuum excess in Fig. 1, where the spectrum is plotted both in linear (top panel) and logarithmic (bottom panel) scales. To demonstrate the significance of the excess, we fit two power-law functions to the continuum excluding major emission lines (with at least ~ 30 Å space around each emission line) and the excess region and the excess region only.

The best-fitting power-law functions follow $F_\lambda \propto \lambda^{-2.21\pm0.04}$ for the majority of the continuum, and $F_\lambda \propto \lambda^{-0.86\pm0.22}$ for the excess region. Although the pixelwise differences between the continuum excess and the power law followed by the majority of the continuum are mostly on the level of 1σ, the cumulative difference over the 550 Å spectral window of the continuum excess is 7.8σ. In comparison, if we evaluate the continuum excess at $2000 - 2500$ Å with the same method, the significance at this regime is only $0.2\sigma - 0.8\sigma$ depending on whether the excess is calculated over the same power law or over a different power law fitted by excluding the $2000 - 2500$ Å spectral region. To check whether the bump is driven by any artefact in observations, we Jackknifed the Prism spectra using individual measurements and still found significant continuum excess. We show the Jackknifed spectra in Appendix A.

In the next section, we outline our method to fit different continuum components in the Prism spectrum of GN-z11 and evaluate the

---

[1] We note that this effect of the correlated noise is not taken into account by other pipelines, which therefore produce NIRSpec spectra which typically have, only apparently, lower noise.

[2] The scaling factor of $2\sqrt{2}$ is motivated by the fact that the total noise has been enlarged by a factor of $\sqrt{2}$ after adding noise to the observed spectrum.

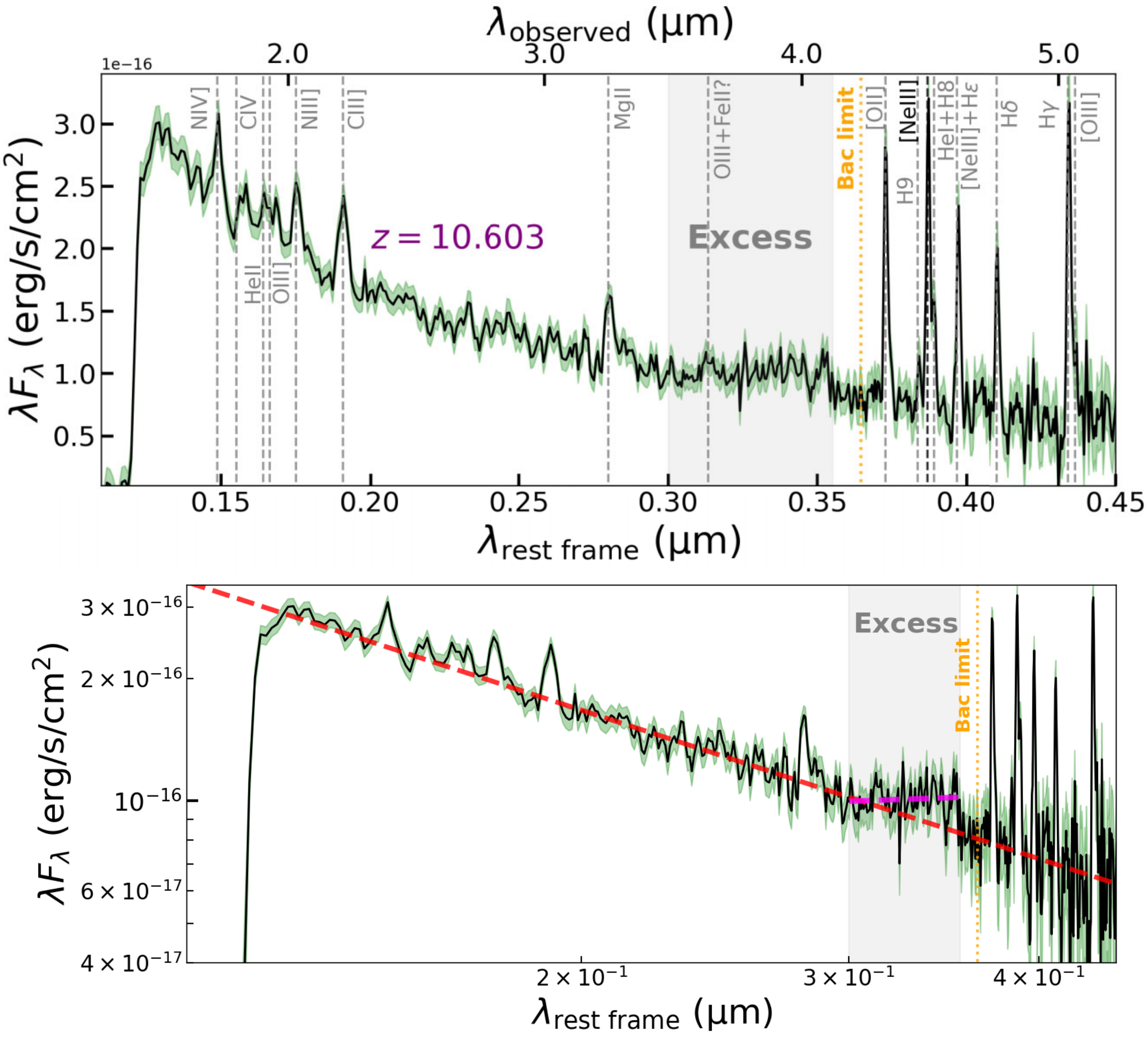

Figure 1. Top: NIRSpec/Prism spectrum of GN-z11. Locations of detected UV and optical emission lines are marked by vertical dashed grey lines. Near the location of C IV, there are both a blueshifted absorption trough and a redshifted emission feature, indicating the presence of outflow if the UV continuum of GN-z11 is AGN dominated (Maiolino et al. 2024a). The grey shaded band indicates the visually identified spectral region showing continuum excess. The orange dotted line indicates the location of the Balmer continuum (Bac) limit at 3646 Å. Bottom: the same spectrum plotted on a log scale. We also plotted two power-law functions that fit the spectrum excluding major emission lines and the continuum excess (red dashed line) and the continuum excess only (magenta dashed line), respectively.

goodness of fits based on different assumptions. We examined different explanations for the presence of the continuum excess, including a Balmer continuum and an Fe II pesudo-continuum.

4 METHODOLOGY

To characterize the observed UV continuum of GN-z11, we considered three major components summarized below. The fits we performed can be broadly divided into two categories under two different assumptions, which are an AGN-dominated UV continuum and an SF-dominated UV continuum, respectively.

(i) A smooth continuum corresponding to the thermal emission from the AGN accretion disc (the 'big blue bump') or the UV continuum of young stellar populations. We considered two physically motivated choices for modelling the continuum. One choice is AGN spectral energy distributions (SEDs) parametrized by black hole masses and Eddington ratios computed by Pezzulli et al. (2017), where we used the SED with a black hole mass of $M_{\rm BH} = 10^6\,{\rm M}_\odot$ and an Eddington ratio of $\lambda_{\rm Edd} \equiv L_{\rm bol}/L_{\rm Edd} = 1$ matching the parameter space estimated by Maiolino et al. (2024a) for GN-z11. We note that varying the black hole parameters in a range of $M_{\rm BH} = 10^{6-7}\,{\rm M}_\odot$ and $\lambda_{\rm Edd} = 1 - 10$ does not significantly change the continuum fitting results (Fabian et al., in preparation). The other choice is the stellar SED fitted by Tacchella et al. (2023b) for the extended component in GN-z11 using photometric data from NIRCam, which is likely associated with the stellar population in GN-z11 and contributes roughly 1/3 of the total fluxes in the rest-frame UV (Tacchella et al. 2023b; Maiolino et al. 2024a). This part of the extended emission

Table 2. Fluxes measured from the Prism spectrum of GN-z11.

Line	Wavelength [Å]	Flux [10^{-20} erg s^{-1} cm^{-2}]
N IV]	1483.98, 1487.15	100 ± 11
He II + O III]	1641.03–1666.76	71 ± 12
N III]	1747.44–1752.77	87.0 ± 8.2
C III] + Si III]	1883.34–1909.37	113 ± 9
[O III] (tentative)	2321.66	18.2 ± 5.1
Mg II	2796.35, 2803.53	54.3 ± 4.0
O III (tentative)	3133.70	8.5 ± 2.7
[O II]	3727.09, 3729.88	92.5 ± 3.9
H9	3836.48	11.8 ± 2.9
[Ne III]	3869.86	98.4 ± 3.8
He I + H8	3889.74, 3890.16	32.9 ± 3.5
[Ne III] + Hϵ	3968.59, 3971.20	61.5 ± 3.8
Hδ	4102.90	49.4 ± 3.5
Hγ	4341.69	93.6 ± 4.8
[O III]	4364.44	21.4 ± 4.4

is likely outside the MSA (and not accounted for by the slit losses). This choice is to test the scenario where the point source component that dominates the MSA observations also has a stellar origin in the UV, although we note that this is in disagreement with the emission-line analyses by Maiolino et al. (2024a). For the AGN and SF SED models above, we set their normalization as a free parameter during the fits. In Appendix B, we also discuss fits assuming a power-law continuum that does not distinguish between the AGN and SF scenarios.

(ii) A nebular continuum including a hydrogen free-bound continuum (with a Balmer continuum truncated at 3646 Å) and a two-photon continuum. The nebular continuum is computed with PYNEB (Luridiana, Morisset & Shaw 2015; Morisset et al. 2020) assuming a range of temperatures of 6×10^3 K $< T_e < 3 \times 10^4$ K and a fixed density of $n_e = 100$ cm^{-3}. While the UV continua of early galaxies might have strong contributions from two-photon emission (e.g. Cameron et al. 2024), based on the high electron density inferred from N III] and N IV] lines ($n_e \gtrsim 10^9$ cm^{-3}, Maiolino et al. 2024a), the ionized gas producing these UV lines should not

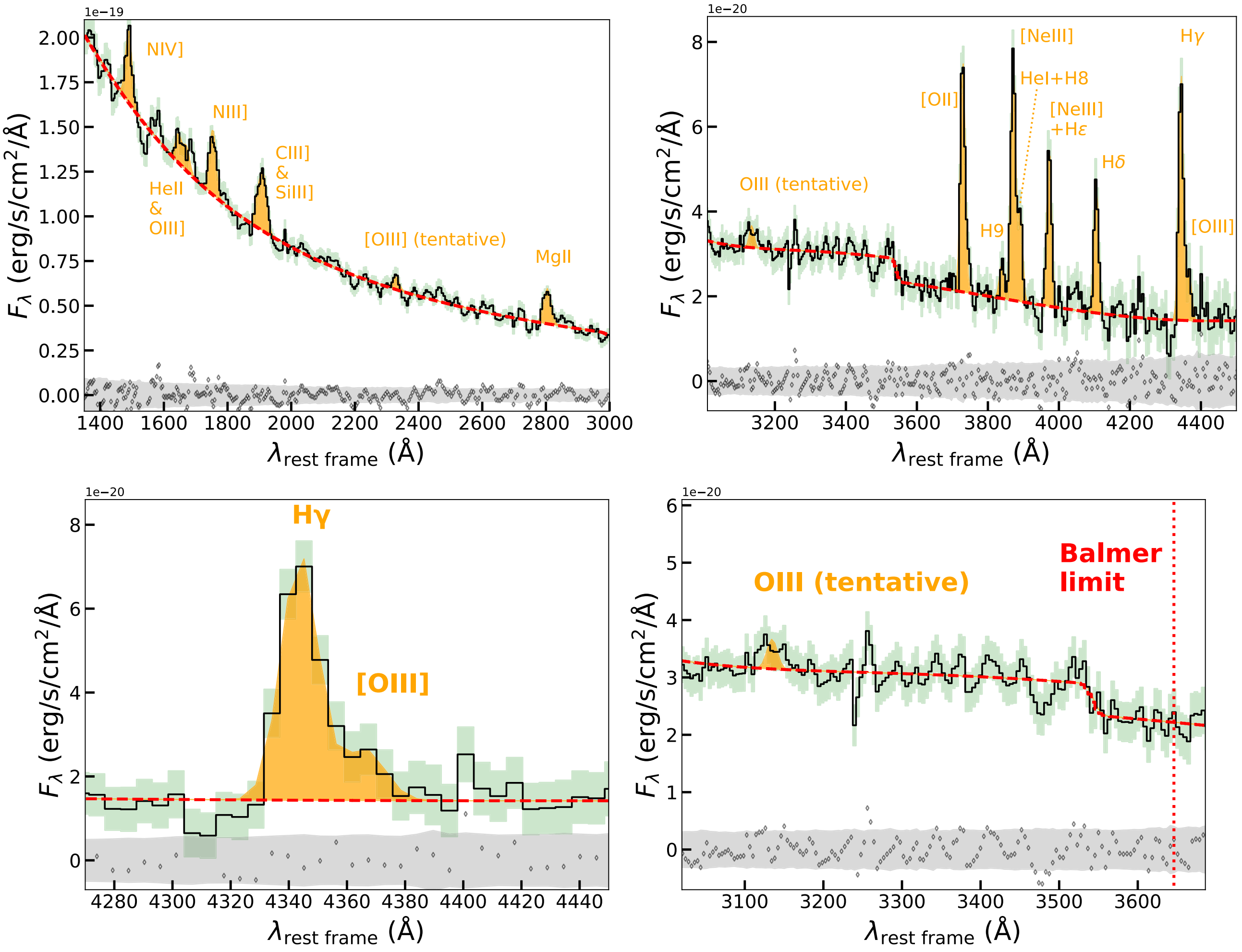

Figure 2. Spectral fitting results from PPXF. The solid black line and the green shaded region represent the observed Prism spectrum and spectral uncertainties of GN-z11 logarithmically rebinned by PPXF. The dashed line is the best-fitting continuum model with a functional form of a fourth-order polynomial. The orange shaded areas correspond to emission-line models. The grey band represents the 1σ rebinned uncertainties and the open diamonds are the fitting residuals. Top left: fitting results for the spectral range of 1350–3000 Å in the rest frame of GN-z11. Top right: fitting results for the spectral range of 3000–4550 Å in the rest frame of GN-z11. Top right: fitting results around Hγ. Bottom: fitting results in the rest-frame near UV. The vertical dotted line indicates the Balmer limit.

Table 3. Input parameters for CLOUDY Fe II models.

Parameter	Values
SED	$T_{\rm BB} = 10^6$ K, $\alpha_{\rm ox} = -1.8$, $\alpha_{\rm uv} = -0.5$, $\alpha_{\rm x} = -1.0$
$\log(U)$	−3.5, −3.0, −2.5, −2.0, −1.5, −1.0
$\log(Z/Z_\odot)$	−2, −1.5, −1, −0.5, 0.0, 0.5
Solar abundance set	Grevesse et al. (2010) solar abundance set
$\log(n_{\rm H}/{\rm cm}^{-3})$	8, 9, 10, 11, 12
Geometry	Plane-parallel; $\log(N_{\rm H}/{\rm cm}^{-2}) = 21 - 25$
Turbulence $v_{\rm turb}/({\rm km/s})$	100, 200, 300, 400, 500, 600
Dust	No dust and no depletion onto dust

have a strong two-photon continuum, which has a critical density of $n_e \sim 10^3$ cm^{-3}. Also, the observed F_λ of GN-z11 does not peak at ~ 1430 Å as would be the case if a two-photon continuum dominated the UV spectrum (Gaskell 1980). Regardless, there could still be two-photon emission from low-density regions (Byler et al. 2017) and we computed it consistently with the H I free-bound continuum under the same nebular conditions. In Appendix B, we discuss the fits with alternative nebular continuum models. The dominant part of the H I free-bound continuum is the Balmer continuum, which can be described by the parametric form of Grandi (1982)

$$F_\lambda = F_\lambda^{\rm BE}\left(\frac{\lambda_{\rm BE}}{\lambda}\right)^2 e^{-\frac{hc}{k_B T_e}\left(\frac{1}{\lambda}-\frac{1}{\lambda_{\rm BE}}\right)}\ ; \lambda \leq \lambda_{\rm BE}, \tag{1}$$

where BE means the Balmer continuum edge and $\lambda_{\rm BE} = 3646$ Å. The only free parameter is the electron temperature, T_e. At fixed T_e, the flux at the Balmer edge, $F_\lambda^{\rm BE}$, is set by the measured fluxes of Balmer lines. In our case, we used the strongest available Balmer line, Hγ, to normalize the free-bound continuum at given temperatures. We note that in previous studies of local nebulae, the flux of H11 ($\lambda_0 = 3771$ Å) is often used to normalize the Balmer jump due to their close proximity in the wavelength space hence insensitivity to dust attenuation (e.g. Liu et al. 2001). From Table 2, the flux ratio of Hγ/H$\delta = 0.53 \pm 0.05$ is consistent with the Case B ratio of 0.55 at $T_e \approx 10^4$ K and $n_e \approx 10^3$ cm^{-3} (Draine 2011). Therefore, the Balmer emission of GN-z11 indicates little or no dust attenuation, consistent with the previous finding of Bunker et al. (2023) based on the observations on 2023 February.

We discuss an alternative choice of a partially optically thick Balmer continuum as initially suggested by Grandi (1982) for fitting quasar spectra specifically in Appendix B.

We note that our main conclusions do not depend on the choice of the Balmer continuum model.

(iii) An Fe II complex in the UV. We computed CLOUDY (v17.03, Ferland et al. 2017; Sarkar et al. 2021) Fe II models assuming a range of parameters listed in Table 3, which are typical parameters used to model nebular emission from BLRs (e.g. Verner et al. 1999; Baldwin et al. 2004; Ferland et al. 2009; Sarkar et al. 2021). We describe the model assumptions in detail in Section 6.3. In brief, we used a standard AGN SED with a big blue bump temperature of $T_{BB} = 10^6$ K, a UV-to-X-ray slope of $\alpha_{\rm ox} = -1.8$, a UV slope of $\alpha_{\rm uv} = -0.5$, and an X-ray slope of $\alpha_{\rm x} = -1.0$. The full SED is described by the following function

$$F_\nu = \nu^{\alpha_{\rm uv}} \exp(-h\nu/kT_{BB}) \exp(0.01\ {\rm Ryd}/h\nu) + a\nu^{\alpha_{\rm x}}, \tag{2}$$

where a is automatically adjusted by CLOUDY to produce the preset $\alpha_{\rm ox}$. We varied the ionization parameter, U, defined as the dimensionless ratio between the flux of the hydrogen ionizing photons and the hydrogen density, from $10^{-3.5}$ to $10^{-1.0}$. We varied the overall chemical abundances from 1 per cent of solar values to three times solar values, assuming the Grevesse et al. (2010) solar abundance set.[3] The hydrogen density covers a range from 10^8 to 10^{12} cm^{-3}, and the hydrogen column density ranges from 10^{21} to 10^{25} cm^{-2}. These values are typical of the BLR clouds or their vicinity, and are those that can provide significant Fe II emission. According to Baldwin et al. (2004), a microturbulence velocity > 100 km s^{-1} is usually needed to describe the Fe II emission in AGNs. The main role of microturbulence is to increase the escape fraction of line photons and increase the strength of continuum pumping, which can increase the equivalent width (EW) of the Fe II emission and smooth the Fe II pseudo-continuum. We considered a broad range for the miroturbulence velocity from 100 to 600 km s^{-1} possible for the BLR in GN-z11 (Bottorff et al. 2000; Maiolino et al. 2024a). Finally, we assume the Fe II-emitting region to lie within the dust sublimation radius and thus has no dust.

To evaluate the effect of different components, we performed two sets of fits. In the first set, we only considered a smooth component (i.e. AGN or SF SED models) and nebular continuum. In the second set, we added the Fe II emission. During these fits, we used the emission-line-subtracted continuum based on our emission-line models shown in Fig. 2. The continuum and pesudo-continuum models were first convolved by the LSF from Graaff et al. (2024) and then resampled to the wavelength grid of the Prism spectrum of GN-z11. We note that the unresolved higher order Balmer lines that are not subtracted ($n > 9$) would reach an intensity similar to the Balmer edge at 3646 Å, making the Balmer jump hardly visible at 3646 Å (Wills et al. 1985). Therefore, the apparent location of the Balmer jump might be slightly redshifted due to the blending of lines with the Balmer edge, but not blueshifted (see e.g. Cameron et al. 2024; Tacchella et al. 2025).

5 CONSTRAINTS ON THE BALMER CONTINUUM

To fit the continuum spectrum, we performed a Markov Chain Monte Carlo calculation using the PYTHON EMCEE package (Foreman-Mackey et al. 2013). We used the following likelihood function

$$\log L = \sum_\lambda -0.5(F_\lambda^{\rm cont.} + F_\lambda^{\rm neb.} - F_\lambda)^2/\sigma_\lambda^2. \tag{3}$$

In the equation above, $F_\lambda^{\rm cont.}$ is the continuum of the AGN accretion disc or stellar populations, $F_\lambda^{\rm neb.}$ is the nebular continuum, F_λ is the observed flux, and σ_λ is the uncertainty of the observed flux. We set flat priors for all model parameters and ran a 5000-step chain for each trial. For each chain, we removed the first 150 steps and resampled the chain with an interval of 50 steps, which is larger than the autocorrelation times of all parameters. The posterior distributions of the parameters were then extracted from the resampled chains.

5.1 Optically thin Balmer continuum case

5.1.1 Balmer jump temperature

In the first fit, we assumed an optically thin Balmer continuum. During the fit, there are two free parameters: the normalization of the AGN or SF continuum model, m, and the electron temperature for

---

[3] Although the abundance pattern in GN-z11 is likely different from the solar abundance pattern (Cameron et al. 2023a), we found the most important elemental abundance in our models is the relative abundance of Fe.

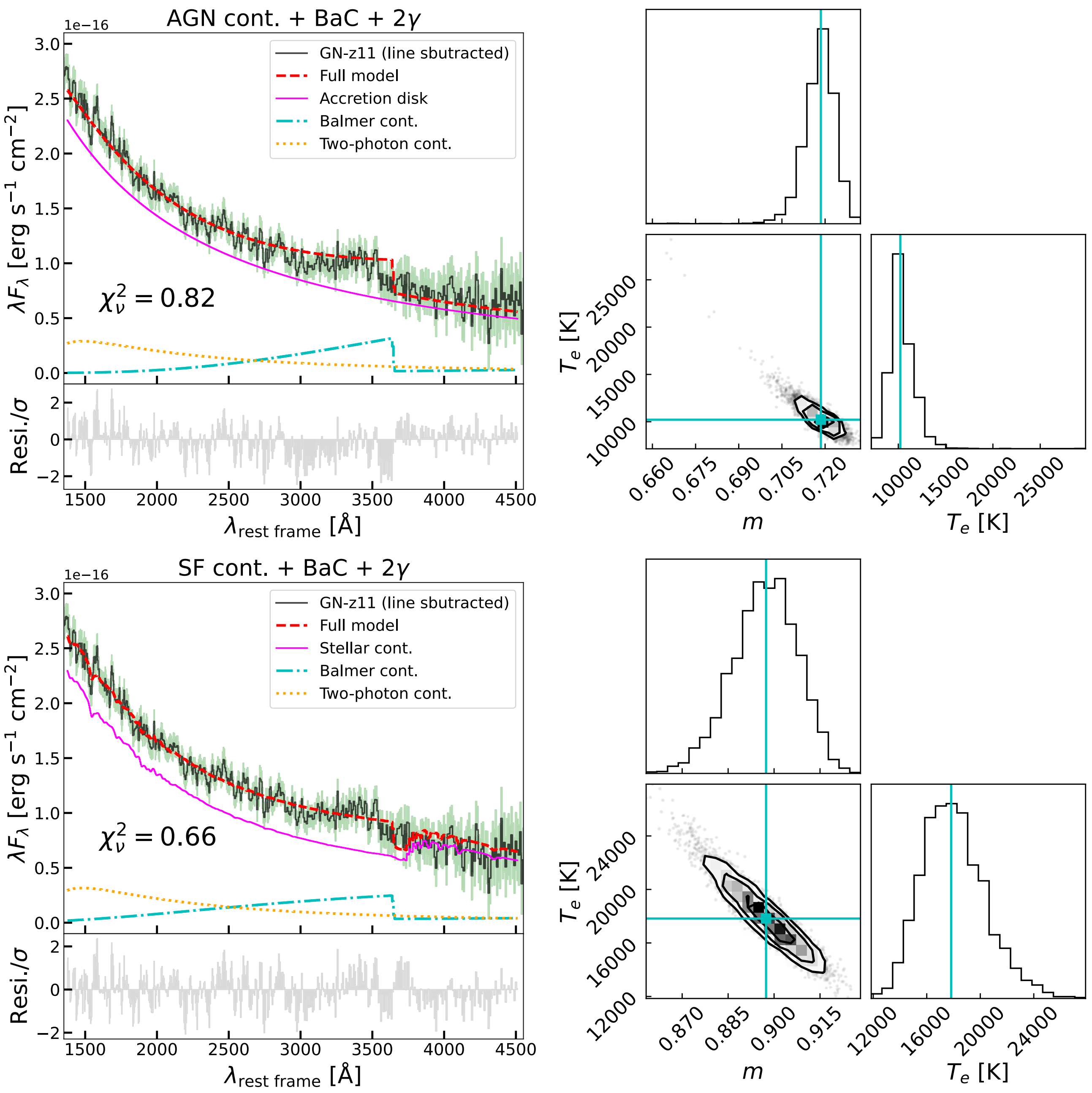

Figure 3. Left columns: best-fitting continuum models for the line-subtracted Prism spectrum (from PPXF) of GN-z11. The corresponding reduced χ^2 are also shown. The fitting residuals normalized by the flux uncertainties are shown in the bottom. Right columns: posterior distributions of model parameters, including the electron temperature of the nebular continuum, T_e, and the normalization of the AGN or SF continuum model, m. The AGN and SF models are first normalized to the Prism flux of GN-z11 at $\lambda = 4260$ Å in the rest frame and then multiplied by m. The vertical cyan lines mark the median of the model parameters, which were taken as the best-fitting parameters. Regardless of the origin of the observed continuum, a significant excess in the near UV (in these cases dominated by the Balmer continuum) is preferred by both fits.

the nebular continuum, T_e. We note that the AGN and SF models are first normalized to the observed Prism flux of GN-z11 at $\lambda = 4260$ Å avoiding major emission lines in the rest frame, and then multiplied by m. We assumed flat priors for these parameters.

We plotted our best-fitting model in Fig. 3, and list the model parameters as well as the corresponding 1σ uncertainties estimated from the posterior distributions in Table 4. Both fits prefer excess fluxes in the near UV, which, in these cases, are interpreted as mainly the Balmer continuum (dash–dotted cyan curves). The AGN continuum produces a larger reduced χ^2 compared to the SF continuum, but we caution that the hyper parameters that produce these continua are not taken into account during the fits. In addition, all reduced χ^2 calculated are less than 1, implying the flux uncertainties might be overestimated (Bevington & Robinson 2003). The AGN continuum fit also prefers a stronger Balmer jump. Based on the AGN continuum model, the best-fitting temperature is $T_e = 1.02^{+0.14}_{-0.09} \times 10^4$ K. The stellar continuum model, on the other hand, gives a higher best-fitting temperature of $T_e = 1.78^{+0.25}_{-0.21} \times 10^4$ K associated with a weaker

Table 4. Best-fitting model parameters for the Prism spectrum of GN-z11 under different assumptions. Among the parameters listed, m is the normalization of the continuum, T_e is the electron temperature of the nebular continuum, and $\lambda_{\rm BE}$ is the wavelength of the Balmer continuum edge. For reference, the temperature measured from emission lines is $T_e = 1.36 \pm 0.13 \times 10^4$ K and the theoretical Balmer edge is at $\lambda_{\rm BE} = 3646$ Å.

AGN ($M_{\rm BH} = 10^6$ M$_\odot$, $\lambda_{\rm Edd} = 1$) + nebular continuum; $\chi^2_\nu = 0.82$			
Parameter	m	T_e [10^4 K]	
Value	$0.719^{+0.004}_{-0.006}$	$1.02^{+0.14}_{-0.09}$	
AGN ($M_{\rm BH} = 10^6$ M$_\odot$, $\lambda_{\rm Edd} = 1$) + nebular continuum (free Balmer continuum edge); $\chi^2_\nu = 0.73$			
Parameter	m	T_e [10^4 K]	$\lambda_{\rm BE}$ [Å]
Value	$0.733^{+0.003}_{-0.003}$	$0.65^{+0.07}_{-0.04}$	3543^{+7}_{-5}
SF + nebular continuum; $\chi^2_\nu = 0.66$			
Parameter	m	T_e [10^4 K]	
Value	$0.90^{+0.01}_{-0.01}$	$1.78^{+0.25}_{-0.21}$	
SF + nebular continuum (free Balmer continuum edge); $\chi^2_\nu = 0.67$			
Parameter	m	T_e [10^4 K]	$\lambda_{\rm BE}$ [Å]
Value	$0.91^{+0.01}_{-0.01}$	$1.60^{+0.26}_{-0.20}$	3601^{+67}_{-36}

jump. The difference between the two fits is mainly driven by the small Balmer break in the stellar continuum model that allows for a larger fraction of the UV light to be contributed by nebular continuum.

We compared the Balmer continuum temperature, $T_e(\mathrm{H}^+)$, with the temperature estimated from the auroral line [O III]λ4363, $T_e(\mathrm{O}^{2+})$. We compared three different methods to estimate the temperature. The first two methods used MSA spectra from JADES. First, we used the empirical relations between [Ne III]λ3869/[O II]λλ3726, 3729 and [O III]λ5007/[O II]λλ3726, 3729 fitted by Witstok et al. (2021) to estimate the flux of [O III]λ5007.[4] The empirical relations were calibrated using SF galaxies and Seyferts from the Sloan Digital Sky Survey (SDSS, York et al. 2000). We thereby predicted the strengths of [O III]λ5007 assuming an SF origin and a Seyfert origin separately. Then, we estimated [O III]λ4363/[O III]λ5007, and we used PyNeb to compute the temperature at the low-density limit as the lines we used mainly come from forbidden transitions of O^{2+}. The estimated temperatures are $T_e(\mathrm{O}^{2+}) = 1.28^{+0.10}_{-0.12} \times 10^4$ K for an SF origin and $T_e(\mathrm{O}^{2+}) = 1.33^{+0.11}_{-0.13} \times 10^4$ K for an AGN origin, which are consistent with the estimation of Cameron et al. (2023a). Second, we used the flux ratio of O III]λλ1661, 1666/[O III]λ4363 to infer the electron temperature. In the Prism spectrum, the blend He IIλ1640 + O III]λλ1661, 1666 is marginally resolved at a spectral resolution of roughly 18 Å at the central wavelength of the blend. If we assume He II and O III] have the same kinematics, our fit gives $F_{\rm OIII]} = 3.35 \pm 0.81 \times 10^{-19}$ erg s^{-1} cm^{-2}. Combining this value with the flux of [O III]λ4363 (Table 2), at the low-density limit ($n_e < 10^4$ cm^{-3}), we obtained $T_e(\mathrm{O}^{2+}) = 1.25^{+0.30}_{-0.16} \times 10^4$ K with PyNeb, consistent with the values derived from the first method. We note that Bunker et al. (2023) reported detection of resolved He II and O III] in the (central 3-pixel extraction) medium resolution ($R \sim 1000$) spectrum with $F_{\rm HeII} = 4.2 \pm 1.3 \times 10^{-19}$ erg s^{-1} cm^{-2}and $F_{\rm OIII]} = 4.3 \pm 1.5 \times 10^{-19}$ erg s^{-1} cm^{-2}. If we took the flux ratio of He II and O III] given by Bunker et al. (2023) to deblend He II + O III] and combined it with the [O III]λ4363 flux we measured, we obtained $T_e(\mathrm{O}^{2+}) = 1.29^{+0.26}_{-0.23} \times 10^4$ K, again consistent with the values using other methods. We also note that there is a detection of a line at $\lambda \approx 2321$ Å in the rest frame, which might be matched with the auroral line [O III]λ2320. Both [O III]λ4363 and [O III]λ2320 are produced from the same upper level and they should have a fixed flux ratio of roughly 4:1. However, in Table 2, one can see the flux ratio is roughly 1:1 and is inconsistent with the expectation, meaning the identification of [O III]λ2320 might not be exact. Therefore, we did not use [O III]λ2320 to infer the electron temperature. Finally, we note that Álvarez-Márquez et al. (2025) recently reported [O III]λ5007 measured in the *JWST*/MIRI MRS spectrum for GN-z11. They derived a temperature of $T_e = 1.40 \pm 0.21 \times 10^4$ K by combining their measured flux for [O III]λ5007 and the flux of [O III]λ4363 reported by Bunker et al. (2023). For consistency, we rederived the temperature with PyNeb using our measured [O III]λ4363 flux and obtained $T_e = 1.36 \pm 0.13 \times 10^4$ K, where the small difference comes from the slightly lower [O III]λ4363 flux we measured. Overall the above temperatures are consistent within 1σ and we took $T_e = 1.36 \pm 0.13 \times 10^4$ K as our fiducial value.

In the case of an AGN-dominated continuum, $T_e(\mathrm{H}^+)$ is lower than $T_e(\mathrm{O}^{2+})$ by $\sim 1.8\sigma$. While the difference is insignificant, it has been observed in local H II regions that the recombination line temperatures are systematically lower than the collisionally excited line temperatures, possibly due to temperature inhomogeneities in the ionized gas (Peimbert 1967; Peimbert et al. 2017). In the case of an SF-dominated continuum, $T_e(\mathrm{H}^+)$ is higher than $T_e(\mathrm{O}^{2+})$ by $\sim 1.7\sigma$. A higher recombination line temperature is usually not expected as the recombination lines have higher emissivities at lower temperature regions. Still, the difference is less than 3σ and there might be systematic uncertainties associated with the choice of the stellar continuum (Tacchella et al. 2023b). Either case, the existence of a nebular continuum indicates the intrinsic UV continuum of GN-z11 is slightly steeper compared to the observed one, as can be seen in Fig. 3. Also, it appears the actual jump location is slightly blueshifted in the observed spectrum. Indeed, the residuals clearly show a wiggling pattern near the jump. Next, we investigate this shift in the wavelength space.

5.1.2 *Is the Balmer jump shifted from the theoretical limit?*

To check the significance of the shift, we set the location of the Balmer edge as another free parameter during the fit. The fitting result is shown in Fig. 4. Again, we investigated two different scenarios where the UV continuum is dominated by an AGN accretion disc and stellar populations, respectively. For the AGN model, the best-fitting Balmer edge is at $\lambda_{\rm BE} = 3543^{+7}_{-5}$ Å, which is significantly blueshifted from the Balmer limit at 3646 Å. However, the best-fitting model appears to systematically overpredict the fluxes within the continuum excess region. The posterior distribution of T_e also hits the lower boundary of 6000 K. The mismatch might be due to the systematics associated with the synthetic AGN SED, or due to the assumption that the nebular continuum is responsible for the continuum excess. Compared to the AGN fitting result in Fig. 3, the χ^2_ν from a free-edge Balmer continuum fit is improved. In addition, we calculated the Bayesian Information Criterion (BIC) of Liddle (2007) defined as

$$\mathrm{BIC} \equiv \chi^2 + \mathrm{k} \ln \mathrm{n}, \tag{4}$$

---

[4] This approach is motivated by the observations that Ne/O remains roughly constant over a wide range of metallicities (Berg et al. 2020) and Ne^+ and O^+ have similar ionization potentials.

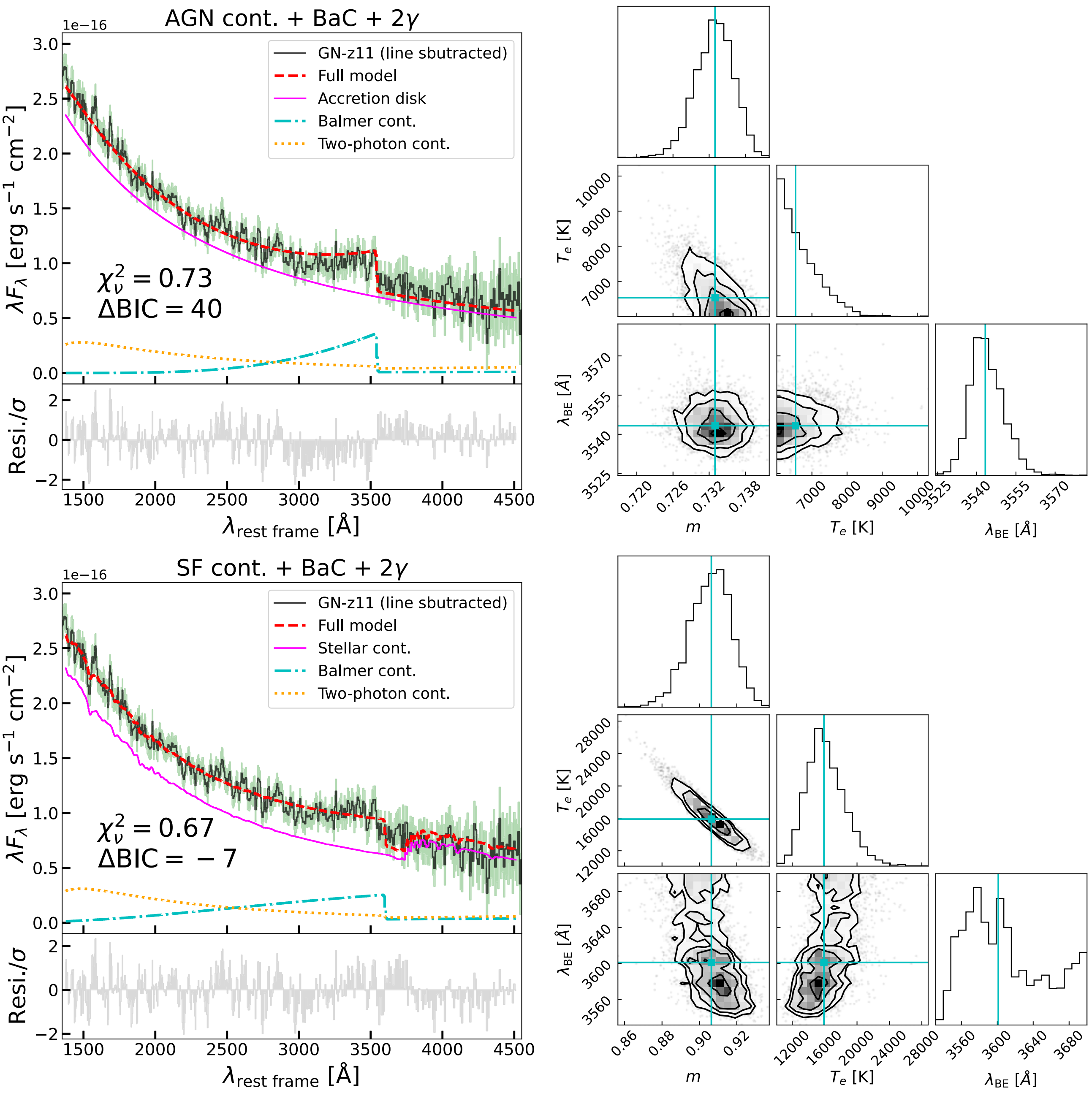

Figure 4. Same as Fig. 3, but making the location of the Balmer continuum edge, λ_{BE}, another free parameter. In the left columns, besides the best-fitting models under the assumptions of an AGN- or SF-dominated continuum, we also show the change in the BIC after adding λ_{BE} as a free parameter. We consider the new fit is significantly better than the old fit only when $\Delta\mathrm{BIC} > 10$. Clearly, in the AGN-continuum scenario, the fit is significantly improved and a blueshifted Balmer edge is preferred. In contrast, in the SF-continuum scenario, the shift in the Balmer edge is not significant due to the presence of a small Balmer break.

where k is the number of free parameters and n is the number of data. We considered $\Delta\mathrm{BIC} > 10$ (i.e. p-value of ~ 0.01; Kass & Raftery 1995) as a requirement for an improved fit with more free model parameters. As a result, adding the Balmer continuum edge as a free parameter gives $\Delta\mathrm{BIC} \approx 40$ for the AGN model, meaning the data do prefer an edge blueshifted from the Balmer limit. The SF fit, on the other hand, does not prefer a significantly blueshifted Balmer edge. As shown in the bottom panels of Fig. 4, the best-fitting SF model has $\lambda_{\mathrm{BE}} = 3601^{+67}_{-31}$ Å. Also, compared to the fit with a fixed Balmer edge, we obtained $\Delta\mathrm{BIC} \approx -7$, which again implies that statistically the non-blueshifted Balmer continuum is preferred by the stellar model. We summarize the values of the best-fitting model parameters from Figs 3 and 4 in Table 4.

As a result, under the assumption of a ‘Balmer continuum-like’ continuum excess, whether the edge of the Balmer continuum is shifted from the theoretical location depends on the prior on the nature of the continuum. If the continuum of GN-z11 is dominated by AGN emission, the continuum excess cannot be reproduced by a typical Balmer continuum as the continuum edge is significantly blueshifted. If the continuum of GN-z11 is dominated by a stellar continuum with a similar shape inferred from the extended component in its image, the continuum excess does not prefer a blueshifted Balmer edge.

5.2 Other possible scenarios involving the Balmer continuum

We also considered the possibility of a partially optically thick Balmer continuum. This model includes an additional free parameter, the optical depth at the Balmer edge, $\tau_{\rm BC}$. We discuss this case in Appendix B. Here, we only summarize that the resulting fits (Fig. B2) have a shape very similar to those with the optically thin case, and plagued by the same issues, with $\tau_{\rm BC}$ being degenerate with the normalization of the continuum and temperature.

From the fits above, one can see the key feature that prevented a good fit with a Balmer continuum model for an AGN-dominated spectrum is around the edge of the small blue bump. We also note that a potential trough centring at ~ 3480 Å (or an emission feature at ~ 3522 Å) and a potential emission feature at ~ 3133 Å cannot be described by the simple continuum model. If we considered a scenario where a Balmer continuum did exist, the question becomes whether to trust a model with a strong jump but somehow blueshifted to around 3550 Å, or a model with a noise-limited weak jump where other emission features dominate the continuum excess.

For the strong-jump scenario, one needs a relatively low temperature and a small optical depth at fixed $F_{\rm H\gamma}$. One might wonder whether a warm cloud in the foreground can absorb part of the Balmer continuum and create the blueshifted jump. Self-absorption of the Balmer emission is unlikely to produce a blueshifted Balmer jump. A potential source of absorption for the Balmer continuum is $\rm Fe^+$ (Wills et al. 1985). However, there is a lack of $\rm Fe^+$ lines between 3550 and 3646 Å. Also, one expects emission from $\rm Fe^+$ rather than absorption in a typical BLR. Alternatively, one might speculate a blueshifted Balmer continuum in a warm outflowing cloud along the line of sight. There are two difficulties with this explanation. First, an ionized cloud with an outflow velocity of ~ 8000 km s^{-1} is required, but there are no blueshifted Balmer lines observed. Second, one expects high order Balmer lines to be blended with the Balmer jump especially given the spectral resolution of Prism.[5] Thus, there should be a smoothly declining edge rather than a sharp truncation even if the Balmer continuum is blueshifted.

5.3 The weak Balmer continuum scenario

For the weak-jump scenario, the Balmer continuum becomes a secondary component and we need an alternative explanation for the continuum excess, which will be discussed in the next sections. If we simply exclude the spectral region between 3000 and 3550 Å (which we will associated with other emission features but keep the region between 3550 and 3646 Å to constrain the strength of the Balmer jump), in the AGN case, the fit (not shown) is significantly worse when the nebular continuum is included ($\chi^2_\nu = 0.80$) compared to when the nebular continuum is not included ($\chi^2_\nu = 0.66$), implying that a suppressed nebular continuum is preferred. In the SF case, on the other hand, the fit (not shown) is significantly better when there is a nebular continuum ($\chi^2_\nu = 0.66$ with the nebular continuum versus $\chi^2_\nu = 1.0$ without the nebular continuum). However, the temperature of the nebular continuum is driven towards $T_e \sim 3 \times 10^4$ K, corresponding to a strongly suppressed Balmer jump. Such a high temperature averaged over $\rm H^+$ is achievable if the ionized gas is either extremely metal-poor and/or the ionizing radiation field is hard enough. As a result, the temperature constraint under the weak-jump scenario provides another piece of evidence on the properties of the ionizing source in GN-z11. As we discuss in Section 7, compared to stellar radiation, ionization from an AGN is easier to achieve this temperature especially given the potentially enriched abundances in GN-z11. We will also discuss that such high temperature is completely inconsistent with the temperature inferred from the forbidden lines (tracing low-density gas), in particular from the [O III]λ4363 auroral line (which gives $T_e = 1.36 \pm 0.13 \times 10^4$ K as discussed above). The only solution in this case is that the bulk of the Balmer emission comes from the high-density gas in the BLR, while the forbidden lines come from the narrow-line region (NLR) or the ISM of the host galaxy.

Alternatively, the Balmer continuum can be suppressed at a lower temperature but with a large optical depth. Both a high ionization parameter and a high density are needed to strongly obscure the Balmer edge. In fact, our CLOUDY models show to produce a similar suppression of the Balmer edge at $T_e \lesssim 20\,000$ K to the optically thin case at $T_e \approx 30\,000$ K, it is critical to have $n \gtrsim 10^6$ cm^{-3}, which is atypical for an ISM origin. Therefore, to produce a suppressed partially optically thick Balmer continuum, one still needs a BLR with AGN ionization.

6 EMISSION-LINE SCENARIOS

6.1 O III Bowen fluorescence

With a weak jump, the next question is the identity of the emission that dominates the small blue bump. It is noteworthy that this continuum excess region is usually lack of strong emission lines. In this wavelength regime, AGNs can show the coronal line [Ne V]λ3426 and the Bowen florescence line O IIIλ3133 (Bowen 1934). There is, however, no detection of [Ne V]λ3426. In contrast, there is potential detection of O IIIλ3133 at a significance of 3.1σ. The resulting flux for this emission feature is $8.5 \pm 2.7 \times 10^{-20}$ erg s^{-1} cm^{-2} (Table 2).

We note that detection of O IIIλ3133 was also reported recently for a *JWST* observed target at $z = 12.34$, GHZ2/GLASS-z12 (Castellano et al. 2024). As we show in Section 6.3, a redshifted Fe II bump can also produce the observed emission at 3133 Å. We further discuss the implication of the emission at 3133 Å in Section 7.

However, we note that the potential O III fluorescence can only account for one of the features seen in the hump.

6.2 Inconsistency with the Wolf–Rayet scenario

Previously, it was also suspected that Wolf–Rayet (WR) stars could be present in GN-z11 and contribute to the chemical enrichment through their powerful winds (Cameron et al. 2023a; Senchyna et al. 2024; Gunawardhana et al. 2025). As shown by the recent results from the UV Legacy Library of Young Stars as Essential Standards program (Bernini-Peron et al. 2024; Roman-Duval et al. 2025), high-ionization P-Cygni profiles (e.g. C IV) caused by stellar winds of metal-poor and massive stars can be strong (i.e. similar to the C IV absorption strength seen in Fig. 1) at ~ 20 per cent solar metallicities. One might wonder whether the emission typically associated with winds from WR stars can produce the continuum excess we see in GN-z11.

It is known that nitrogen sequence WR (WN) stars show strong nitrogen emission lines in the rest-frame UV (Abbott & Conti 1987). In the wavelength range of 3000 Å $< \lambda <$ 3550 Å, the strongest

---

[5] The spectral resolution near the bump is $R \sim 280$ after taking into account the fact that the source is more compact with respect to the width of the shutter (Graaff et al. 2024).

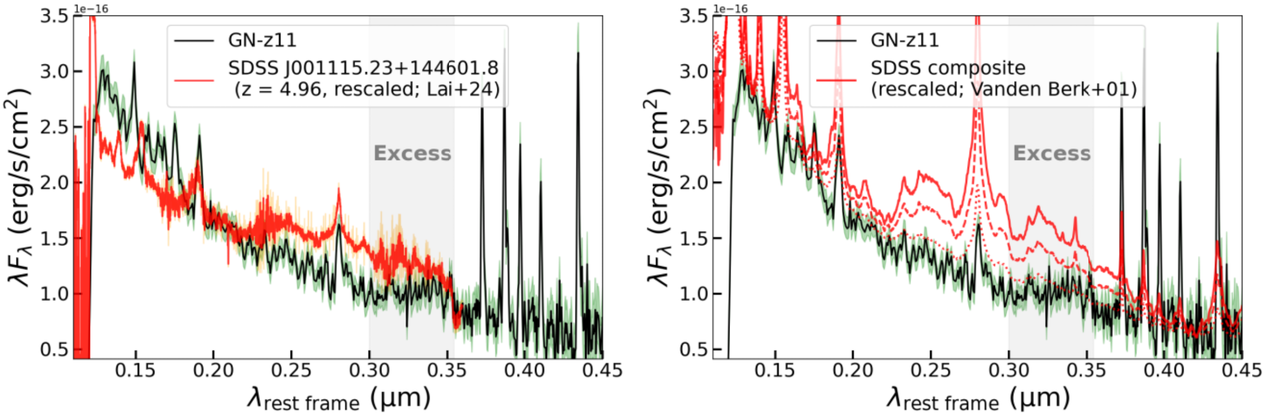

Figure 5. Left: comparison between the rest-frame spectrum of GN-z11 with that of a quasar at $z = 4.96$, SDSS J001115.23 + 144601.8, from the XQz5 catalogue of Lai et al. (2024). The flux of the quasar spectrum is rescaled to compare with the GN-z11 spectrum. The green and the orange shaded regions represent the 1σ uncertainties for the two spectra, respectively. The continuum excess region in GN-z11 is marked by the grey shaded region. Right: comparison between the rest-frame spectrum of GN-z11 with that of a modified composite spectrum constructed from 2200 quasars in SDSS by Vanden Berk et al. (2001). To better compare the nebular emission, the power-law continuum of the composite spectrum has been replaced with the power law we fitted for GN-z11. The dotted, dashed, and solid red lines correspond to different constant scaling factors of 1, 2, and 3 for the normalized nebular emission, respectively. The grey shaded region marks the continuum excess identified in GN-z11.

emission feature in WN stars is usually N IV$\lambda\lambda$3478, 3483 (Garmany, Massey & Conti 1984; Conti & Massey 1989). However, at the expected location of this emission line ($\sim$ 3480Å), there is actually a trough in the continuum excess region in GN-z11. As shown in Fig. 2, there is no individual Gaussian-like component within the continuum excess region comparable to the tentative O IIIλ3133. We tried fitting these strongest WN lines with PPXF and found no detection at $> 3\sigma$. Besides nitrogen lines, broad emission humps around He II lines are expected from the winds of WR stars. Within the spectral range of interest, WR stars can produce emission of He IIλ3204 from the winds (Stanway & Eldridge 2018). Again, there is no detection of He IIλ3204 from our fit in Fig. 2. Thus, it is unlikely that the small blue bump is caused by WN emission.

In addition, as discussed by Maiolino et al. (2024a), the absence of N IVλ1718 in GN-z11, which would be strong in WN stars showing strong N IV]λ1486, further argues against the presence of WR stars. Finally, the medium-resolution rest-frame UV spectrum of GN-z11 combining NIRSpec/MSA and NIRSpec/IFU observations show no detection of any broad He IIλ1640 hump (Maiolino et al., in preparation), which is a typical feature associated with WR winds. This further rules out the possibility that the UV emission of GN-z11 is dominated by WR stars. Next, we discuss in the context of AGN, whether there is other continuum model that can provide a better fit for the spectrum of GN-z11.

6.3 Fe II emission

In a typical BLR, due to the high gas density and the destruction of dust grains, Fe$^+$ can be abundant and produce strong permitted emission lines in the UV. The resulting Fe II emission has been considered as the major contributor to the small blue bumps in quasar spectra. In Fig. 5, we make a direct comparison between the spectrum of GN-z11 and quasar spectra at lower redshifts. In the left panel, we show the spectrum from a luminous quasar at $z = 4.96$ from Lai et al. (2024), where the small blue bump is apparent between 2000 and 3550 Å. Intriguingly, the small blue bump in the quasar shows a truncation just at 3550 Å, similar to the truncation of the continuum excess in GN-z11. This truncation of the small blue bump traces the red end of the UV Fe II complex and is included in empirical UV Fe II templates for quasars (Mejía-Restrepo et al. 2016). The strength of the Fe II emission, however, varies strongly among quasars and the underlying physics remains poorly understood due to the complex production mechanisms and radiative transfer of Fe II lines (see e.g. Baldwin et al. 2004; Ferland et al. 2009; Gaskell et al. 2022, and references therein).

In the right panel of Fig. 5, we show another comparison between an average quasar spectrum constructed by Vanden Berk et al. (2001) and the spectrum of GN-z11. The composite quasar spectrum of Vanden Berk et al. (2001) has a relatively strong and flat continuum. To better compare the jump feature, we replaced the continuum of the composite spectrum with that of GN-z11 and rescaled the strength of the nebular emission. To do this, we first normalized the composite quasar spectrum to the flux density of the GN-z11 spectrum at $\lambda = 2300$ Å. After that, we subtracted the best-fitting power law[6] of Vanden Berk et al. (2001) for the spectral range of 1300 Å $< \lambda <$ 5000 Å, which has a slope of -1.56. We considered that the residual of the quasar spectrum is dominated by nebular emission and, for illustration purposes, multiplied the flux densities by factors of 1, 2, and 3. Finally, we added the rescaled nebular components to the best-fitting power law of the GN-z11 spectrum, which has a slope of -2.36 and plotted them in Fig. 5. The bump between 3000 and 3550 Å is clearly visible in the composite quasar spectrum, although the continuum excess blueward of the small blue bump is stronger. The Fe II jump at $\sim$ 3550 Å is also present, and there is an additional jump likely caused by a Balmer continuum around 3800 Å. In Appendix C, we provide a few other examples of Fe II jumps in observations of individual quasar spectra. A group of Fe II fluorescent lines around 3533 Å is likely responsible for the Fe II jump (Netzer & Wills 1983), although the observed jumps in quasars all appear slightly redshifted to 3550 Å.

---

[6] The best-fitting power law of Vanden Berk et al. (2001) was obtained by dividing the quasar spectrum into segments with longest possible wavelengths whose ends can be connected by power laws without intersecting the spectrum. We refer the readers to section 4.1 of Vanden Berk et al. (2001) for more details.

The apparent difficulty associated with the Fe II explanation for the continuum excess is the atypical shape observed in GN-z11. In Fig. 5, it is clear that Fe II emissions in both quasar spectra have higher fluxes at shorter wavelengths within the continuum excess region. In GN-z11, the 'Fe II complex' is stronger towards the red end instead. One might wonder whether significant internal dust attenuation beyond the dust sublimation radius could produce this shape. While the Balmer decrement is consistent with Case B values, it is possible that the Fe II emission originates from a different ionized region that has dust in the foreground (Shields et al. 2010). However, without an independent way to constrain the dust geometry, this approach gives too much freedom to Fe II models and the resulting optical Fe II emission might become too strong compared to UV Fe II emission. On the other hand, given that the physical conditions in GN-z11 are very different from lower redshift quasars, we considered the possibility of producing a strong Fe II jump by exploring a large grid of dustless CLOUDY photoionization models.

Table 3 summarizes the range of parameters we adopted for the Fe II models. We adopted a standard AGN SED for the ionizing source and a range of ionization parameters typically found in AGN ionized gas. The SED is assumed to have the functional form of equation (2), where the accretion disc temperature is set to $T_{\rm BB} = 10^6$ K, the X-ray slope is set to $\alpha_{\rm x} = -1$, and the UV slope is set to $\alpha_{\rm uv} = -0.5$. Parameter a sets the optical-to-X-ray slope, which is typically $\alpha_{\rm ox} = -1.4$ for local AGN (Zamorani et al. 1981). However, as recently suggested by Lambrides et al. (2024), the intermediate-to-low-luminosity AGN population discovered by *JWST* have $\alpha_{\rm ox} \sim -1.8$ or even lower as they are much weaker in hard X-ray bands compared to the local AGN with similar bolometric luminosities. We checked SEDs with $\alpha_{\rm ox} = -1.2$, -1.4, and -1.8, respectively. The shape of the Fe II emission has a slight dependence on $\alpha_{\rm ox}$. When the optical-to-X-ray slope is steeper, the Fe II emission at $\lambda > 3000$ Å is slightly enhanced with respect to that from the shorter wavelength. We also checked the effect of varying accretion disc temperature. When $T_{\rm BB}$ is decreased to 10^5 K, the change in the relative shape of the Fe II emission is not obvious despite some slight suppression at $\lambda < 2200$ Å and slight enhancement at $\lambda > 3000$ Å. We therefore set $\alpha_{\rm ox} = -1.8$ as the fiducial value, but keep $T_{\rm BB} = 10^6$ K.

For the metallicity, although the estimated oxygen abundance is around 1/10 the solar value based on forbidden lines (Bunker et al. 2023), we considered metallicities up to supersolar values to take into account potential early enrichment of metals in the central region of GN-z11 (Cameron et al. 2023a; Maiolino et al. 2024c), where the Fe II emission originates. To allow strong permitted transitions of Fe^+, it is necessary to have high densities, and thus we set $n_{\rm H} \geq 10^8$ cm^{-3}. In addition, we assumed the gas to be density-bounded as expected for typical BLRs and set the stopping column density, $N_{\rm H}$, to range from 10^{21} to 10^{25} cm^{-2}. Although a hydrogen column density as high as 10^{25} cm^{-2} is atypical for low-z AGNs, such a value might not be uncommon for high-z AGNs that show BLR components in emission lines but lack X-ray emission (Maiolino et al. 2024c). A high column density combined with a high ionization parameter generally boosts Fe II emission due to the extended warm ionized zone with Fe^+. Finally, the microturbulence velocity is an important parameter that changes the strength and shape of the Fe II emission (e.g. Netzer & Wills 1983; Verner et al. 1999). We allowed the microturbulence velocity[7] to vary from 100 to 600 km s^{-1}, encompassing the potential range of gas velocity dispersion in the BLR of GN-z11 probed by N IV]λ1486 ($\sigma = 200 \pm 21$ km s^{-1}; Maiolino et al. 2024a) and He IIλ1640 ($\sigma = 510 \pm 160$ km s^{-1}; Maiolino et al. 2024a).

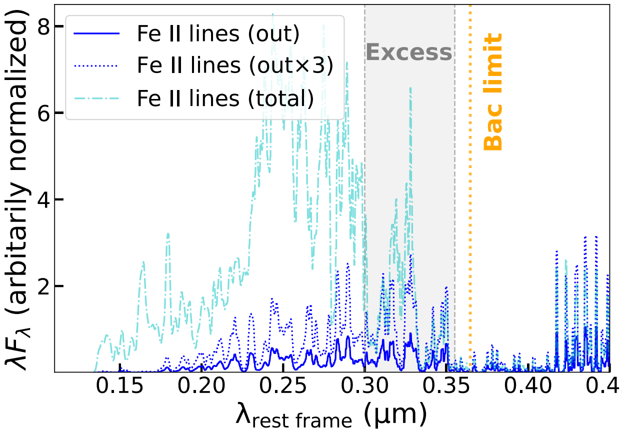

Figure 6. Example of an Fe II pseudo-continuum computed with CLOUDY. The total Fe II emission produced by the simulation is plotted as the dash–dotted cyan line, and the Fe II emission propagated outwards is plotted as the solid blue line. The difference between the two sets of Fe II emission originates from the wavelength-dependent line optical depth, which leads to a more significant reduction of Fe II emission at $\lambda_{\rm rest\ frame} < 3000$ Å. The dotted blue line was obtained by simply scaling up the flux of the outwards Fe II emission by a factor of 3. The grey shaded region indicates the continuum excess region identified in GN-z11. The dotted orange line marks the location of the Balmer limit.

A key mechanism that can produce a strong Fe II jump at ~ 3550 Å relative to the Fe II emission blueward of 3000 Å is the strong dependence of the Fe II optical depth on the wavelength. This generally leads to a greater reduction of the Fe II emission in the shorter wavelength in the emergent spectrum (Ferland et al. 2009). Fig. 6 shows an example of an Fe II model with $\log(U) = -2.5$, $Z = \mathrm{Z}_\odot$, $n_{\rm H} = 10^{11}$ cm^{-3}, $N_{\rm H} = 10^{25}$ cm^{-2}, and $v_{\rm turb} = 300$ km s^{-1}. As pointed out by Ferland et al. (2009), it is important to distinguish the total (intrinsic) Fe II emission from the Fe II emission that is observed. For a typical geometry proposed by Ferland et al. (2009) where the Fe II emission is seen from the back of the BLR clouds (i.e. opposite to the illuminated face), one should consider the portion of the emission that is beamed away from the ionizing source, which we plotted as the emergent or 'out' component. While the total Fe II emission peaks around 2500 Å in the UV, the emergent Fe II emission is stronger in the continuum excess region of GN-z11. Between 3000 and 3550 Å, there are three groups of Fe II emission separated by two gaps in the emergent spectrum, with the rightmost one producing a jump close to the edge of the continuum excess region. We discuss below how flexible the shape of the UV Fe II emission is and whether the range of physical parameters preferred by the observed data is physically plausible.

6.3.1 Parametrization of the shape of the Fe II emission

To characterize the shape of the Fe II complex, we defined two parameters. The first parameter, $r_{\rm uv}$, is defined as

$$r_{\rm uv} \equiv F_{2000\,\text{Å}<\lambda<3000\,\text{Å}}/F_{3000\,\text{Å}<\lambda<3550\,\text{Å}}, \qquad (5)$$

which describes the relative strength of the Fe II pseudo-continuum in the continuum excess region with respect to the part at shorter wavelengths. The second parameter, $r_{\rm bump}$, is defined as

$$r_{\rm bump} \equiv F_{3000\,\text{Å}<\lambda<3550\,\text{Å}}/F_{3400\,\text{Å}<\lambda<3550\,\text{Å}}, \qquad (6)$$

---

[7] We note that in CLOUDY, the turbulence velocity is related to the velocity dispersion by $v_{\rm turb} = \sqrt{2}\sigma$.

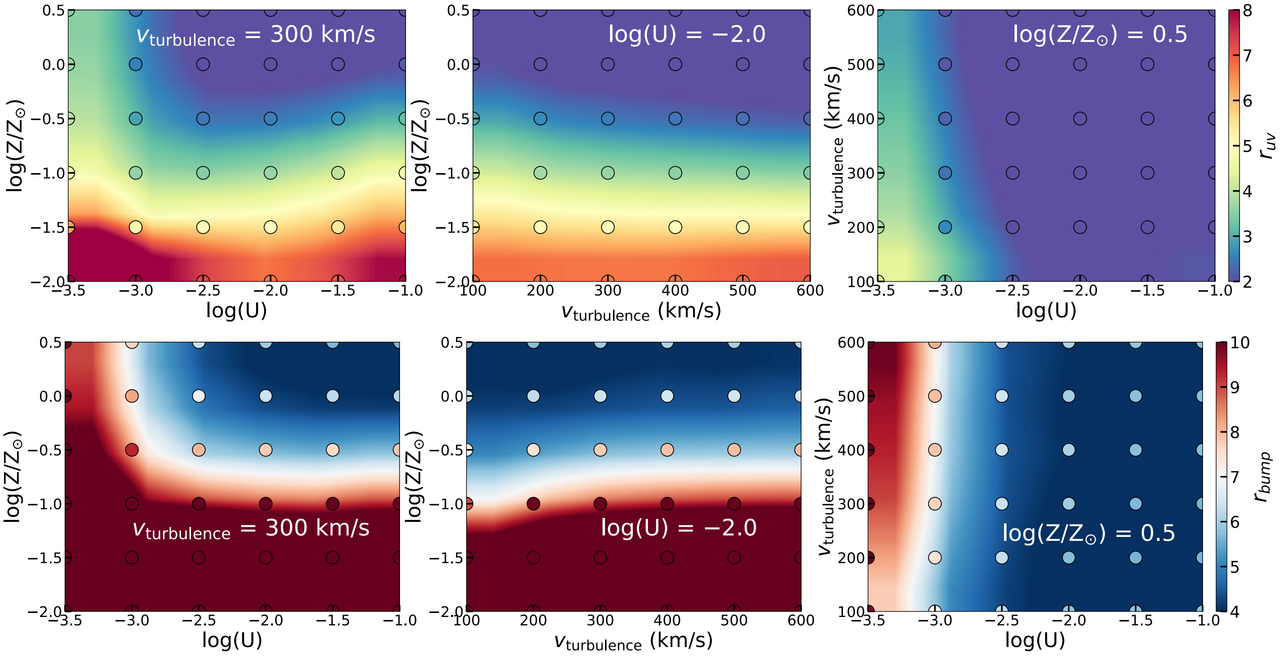

Figure 7. Top: the relative strength of the continuum excess, $r_{\rm uv}$, as functions of the metallicity, ionization parameter, and turbulent velocity. In each panel, we varied two of the three parameters while keeping the third parameter at the value producing the smallest $r_{\rm uv}$ within the range of the parameter space (as shown by the white text in each panel). Individual CLOUDY models are plotted as coloured circles and the background colour maps correspond to 2D linear interpolations of the models. Bottom: the relative strength of the Fe II emission near the jump, $r_{\rm bump}$, as functions of the metallicity, ionization parameter, and turbulent velocity. Definitions of $r_{\rm uv}$ and $r_{\rm bump}$ are given by equations (5) and (6).

which describes the relative strength of the Fe II emission making up the jump compared to the whole Fe II emission in the continuum excess region. As an example, for the model in Fig. 6, $r_{\rm uv} = 1.7$ and $r_{\rm bump} = 4.2$ for the outwards Fe II emission, and $r_{\rm uv} = 6.2$ and $r_{\rm bump} = 8.6$ for the total Fe II emission. Given the shape of the observed continuum excess in GN-z11, we looked for models with both small $r_{\rm uv}$ and small $r_{\rm bump}$.

To investigate the effect of different parameters, we started with a fiducial set of parameters typical for a Compton-thick BLR with $n_{\rm H} = 10^{11}$ cm^{-3} and $N_{\rm H} = 10^{25}$ cm^{-2}, and varied the other three parameters, which are the metallicity, ionization parameter, and turbulent velocity. Within the range of the parameter space we considered, the minimum $r_{\rm uv}$ was found at $\log(U) = -2.0$, $\log(Z/Z_\odot) = 0.5$, and $v_{\rm turb} = 300$ km s^{-1}, and the minimum $r_{\rm bump}$ was found at $\log(U) = -1.0$, $\log(Z/Z_\odot) = 0.5$, and $v_{\rm turb} = 200$ km s^{-1}. While the values of $\log(U)$ and $v_{\rm turb}$ are possible for a highly ionized and turbulent BLR (or one having shears/velocity gradients on small scales; Bottorff et al. 2000), a supersolar metallicity seems too high for a galaxy ~ 430 Myr after the big bang and is in conflict with the subsolar oxygen abundance inferred from forbidden lines (Bunker et al. 2023). Still, based on different model assumptions, the potential range of the metallicity for GN-z11 could reach near-solar or even supersolar values (Isobe et al. 2023; Cameron et al. 2023a), especially in the very small region of the BLR (Maiolino et al. 2024a). We also note that the iron abundance is more important than the overall chemical abundances in these models, meaning a supersolar Fe/H combined with a subsolar metallicity can reproduce these results as well.

Fig. 7 shows the impact of different input parameters on the predicted $r_{\rm uv}$ and $r_{\rm bump}$. We fixed one parameter at the value that produces the minimum $r_{\rm uv}$ or $r_{\rm bump}$, and varied two remaining parameters at a time. The result shows that a metallicity of $\log(Z/Z_\odot) \gtrsim -0.5$ is critical to suppress the UV Fe II emission blueward of the jump while enhancing the apparent jump strength. Meanwhile, an intermediate value of $\log(U)$ and a turbulent velocity of $v_{\rm turb} \gtrsim 200$ km s^{-1} help to achieve the minimum $r_{\rm uv}$ and $r_{\rm bump}$. To check whether our choice of $n_{\rm H} = 10^{11}$ cm^{-3} and $N_{\rm H} = 10^{25}$ cm^{-2} significantly affect the determinations of minimum $r_{\rm uv}$ and $r_{\rm bump}$, we further varied $n_{\rm H}$ and $N_{\rm H}$ over a larger range while keeping $\log(U)$, $\log(Z/Z_\odot)$, and $v_{\rm turb}$ at values producing the minimum $r_{\rm uv}$. Fig. 8 shows the results of varying $n_{\rm H}$ and $N_{\rm H}$. To minimize $r_{\rm uv}$, one needs $n_{\rm H} \gtrsim 10^{10}$ cm^{-3} and $N_{\rm H} \gtrsim 10^{24}$ cm^{-2}. For $r_{\rm bump}$, while the global minimum is at $n_{\rm H} = 10^{8}$ cm^{-3} and $N_{\rm H} = 10^{21}$ cm^{-2}, combined with the constraints from $r_{\rm uv}$, one still needs $n_{\rm H} > 10^{10}$ cm^{-3} and $N_{\rm H} > 10^{24}$ cm^{-2}. The latter implies Compton-thickness, typical of other high-redshift AGNs (Brightman & Ueda 2012; Lanzuisi et al. 2018). The large $n_{\rm H}$ is typical of the BLR clouds. Finally, the high metallicity is also typical of the BLR of AGN, although at such early epochs the very high Fe enrichment might be puzzling, but as much as the high nitrogen enrichment has been puzzling for this and other high-z galaxies (Isobe et al. 2023; Cameron et al. 2023a; Senchyna et al. 2024; Topping et al. 2024). We discuss this point in detail in Section 7.

Issues however remain even if we adopt high-metallicity models. The minimum values of parameters predicted by the models are $r_{\rm uv} = 1.5$ and $r_{\rm bump} = 3.9$. If we fit a power law to the observed spectrum while excluding the bump region, and took the residual as the potential Fe II emission, the corresponding $r_{\rm uv}$ is basically noise-limited and $r_{\rm bump} = 1.1 \pm 0.2$, which are significantly smaller than the model predictions. The differences are in part due to the gaps between groups of Fe II emission in the wavelength space, which are not observed in typical quasar spectra as well as in GN-z11. The absence of the gaps could be a result of broadening by the LSF of the instrument, broadening by the intrinsic velocity dispersion of the

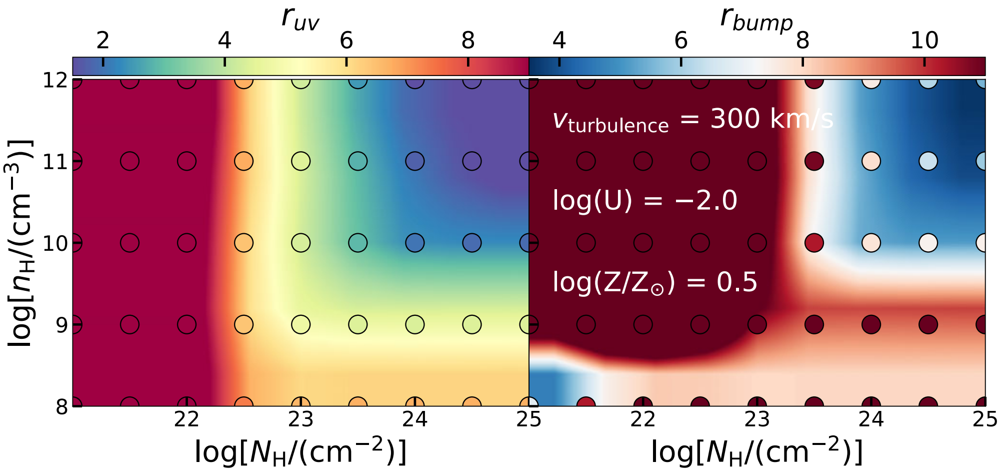

Figure 8. Left: the relative strength of the continuum excess, $r_{\rm uv}$, as a function of the hydrogen volume density and the hydrogen column density. Individual CLOUDY models are plotted as coloured circles and the background colour maps correspond to 2D linear interpolations of the models. Right: the relative strength of the Fe II emission near the jump, $r_{\rm bump}$, as a function of the hydrogen volume density and the hydrogen column density. The metallicity, ionization parameter, and turbulent velocity were fixed at the values producing the smallest $r_{\rm uv}$ within the range of the parameter space. Definitions of $r_{\rm uv}$ and $r_{\rm bump}$ are given by equations (5) and (6).

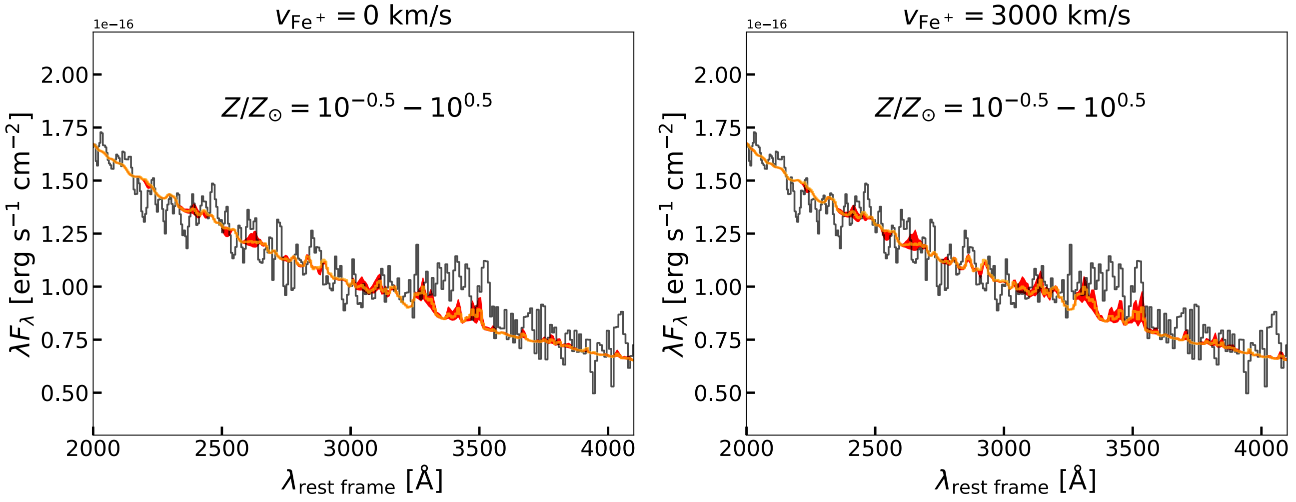

Figure 9. Comparisons between theoretical Fe II models with the observed bump in GN-z11. In each panel, the orange solid line represents an Fe II model with a solar metallicity combined with an AGN continuum model. The red shaded region shows the variation of the Fe II model within a range of metallicities from roughly 1/3 the solar value to three times the solar value (while keeping the normalization of the Fe II model the same). The solid black line is the line-subtracted Prism spectrum of GN-z11 in the rest frame. In the left panel, the relative velocity between the Fe II and the forbidden-line-emitting clouds, $v_{\rm Fe^+}$, is set to 0. In the right panel, however, $v_{\rm Fe^+}$ is set to 3000 km s^{-1} so that the Fe II emission is associated with a fast inflow within the BLR.

BLR, and pumping of unaccounted transitions by nearby lines and continua (Netzer & Wills 1983; Verner et al. 1999; Baldwin et al. 2004; Ferland et al. 2009; Sarkar et al. 2021). Next, we directly compared the models with the bump in GN-z11 taking into account the above effects.

6.3.2 *Comparison with the observed bump*

In Fig. 9, we compare three sets of Fe II models with $\log(Z/Z_\odot) = -0.5$, 0, and 0.5 combined with the fiducial AGN continuum SED we adopted for GN-z11 from Pezzulli et al. (2017). Based on the analysis in the previous subsection, we set $\log(U) = -2.0$, $v_{\rm turb} = 300$ km s^{-1}, $n_{\rm H} = 10^{11}$ cm^{-3}, and $N_{\rm H} = 10^{25}$ cm^{-2} for these models. We set the normalization of the Fe II emission as a free parameter to take into the account the possibility that it arises from a region different from other strong lines in the BLR (e.g. Ferland et al. 2009) and adopted the normalization that best reproduces the small blue bump. Before we made the comparisons, we broadened the Fe II models by an LSF constructed from combining the broadening by the microturbulence in the models and the broadening by the instrumental resolution ($\sim 1.1 \times 10^3$ km s^{-1}).

Finally, judging from Figs 5 and 6, the theoretical Fe II jump generated by CLOUDY is slightly blueshifted compared to the observed jump, meaning the Fe II emission in GN-z11, if it exists, should be redshifted with respect to other strong emission lines. In fact, Fe II emission was often found to be redshifted in quasar spectra at lower redshifts and redshift velocities up to 3000 km s^{-1} were reported previously (Hu et al. 2008a, b). As an example, in Fig. 5 and Fig.

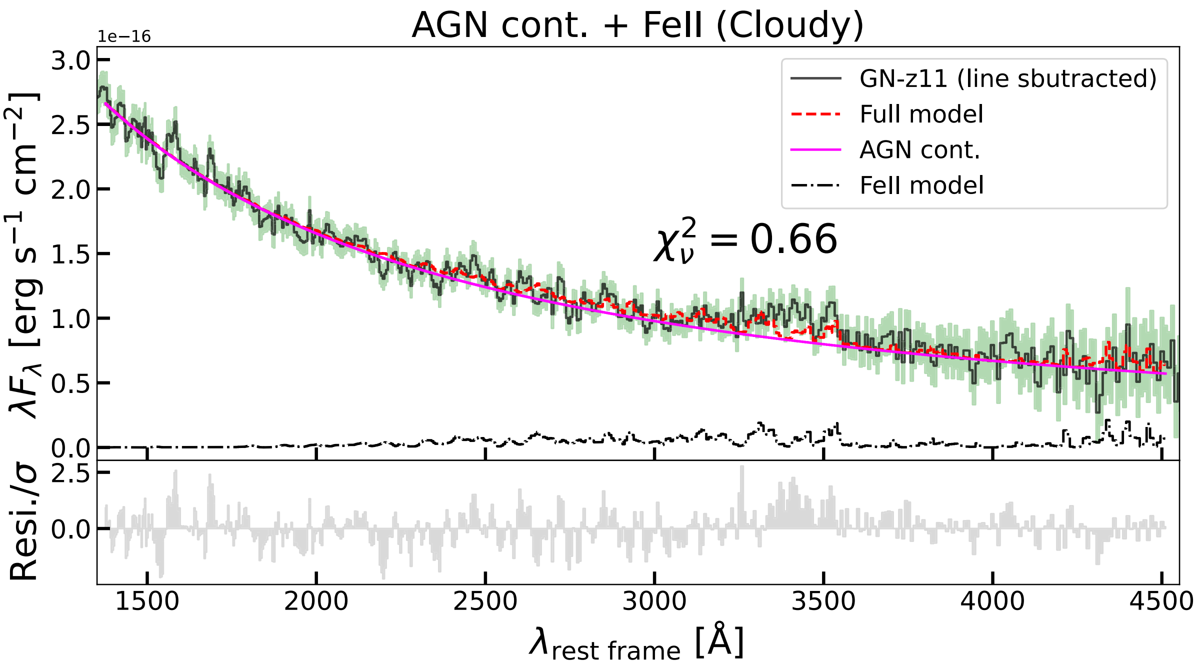

Figure 10. Best-fitting model of an AGN continuum combined with theoretical Fe II emission computed with CLOUDY. The solid black line represents the line-subtracted Prism spectrum of GN-z11. The dashed red line is the full model composed of an AGN continuum (solid magenta) and Fe II emission (dashed black). The relative velocity between the Fe II-emitting clouds and the forbidden-line-emitting clouds, $v_{\rm Fe^+}$, is set to 3000 km s^{-1}. The green shaded region indicates the 1σ uncertainty of the observed flux. The χ residual of the fit is shown in the bottom panel.

C1, the Fe II jumps in these quasars are not significantly blueshifted with respect to the jump seen in GN-z11. We therefore performed a separate comparison using redshifted Fe II models in the right panel of Fig. 9, and further discuss its physical explanation in Section 7.

While compared to the Balmer continuum models in Fig. 3, the Fe II models fail to reproduce the middle part of the small blue bump due to the aforementioned gaps between different groups of Fe II emission, the Fe II models are able to recover certain observed features near the boundaries of the bump. One can see clear Fe II jumps in the models, which match the observed jump increasingly better with increasing metallicity, especially for those models having a velocity shift of $\sim$ 3000 km s^{-1}. On the other hand, the potential emission line at 3133 Å can be explained by a group of redshifted Fe II emission, as shown in the right panel of Fig. 9. In Fig. 10, we compare the highest metallicity Fe II model that produces the strongest UV jump with the observed bump in GN-z11. While the Fe II jump in the model well resembles the observed jump at 3550 Å, the flux of the observed bump between 3300 and 3480 Å is clearly underestimated by the model. Still, the best-fitting Fe II + AGN model outperforms other AGN fits by giving $\chi^2_\nu = 0.66$, which is similar to the χ^2_ν from the best-fitting SF model with a nebular continuum.

The question now becomes whether it is possible to fill the gaps between the Fe II emission. In Fig. 5, the Fe II emission in quasars does not exhibit noticeable gaps in the continuum excess region. If the absence of gaps is purely due to the broadening of Fe II line profiles, one needs an intrinsic FWHM $\gtrsim 8 \times 10^3$ km s^{-1}. Although with a larger microturbulence velocity, the Fe II emission in the continuum excess region would become even stronger with respect to the Fe II emission at shorter wavelengths (and thus produce a stronger bump), the required broadening is significantly larger than the measured widths of semiforbidden lines and permitted lines in GN-z11, which presumably come from the same BLR that produces the Fe II emission.

Alternatively, one might wonder whether any unaccounted line/continuum fluorescence of the Fe II emission between the gaps could explain the model mismatch. Indeed, from the observed high-resolution quasar spectra as well as the empirical Fe II templates constructed from them, the gaps we see in the models are also filled with lines (e.g. Tsuzuki et al. 2006; Mejía-Restrepo et al. 2016). Thus, it is possible that our current models still do not fully capture the fluorescence of the Fe II emission between 3000 and 3550 Å. A full scrutiny of the physical processes in Fe II modelling is beyond the scope of this work and we leave the theoretical calculation of the Fe II emission under extreme physical conditions for future investigations. In what follows, we simply consider the Fe II emission as a candidate to produce the jump feature while discussing the physical interpretations.

7 DISCUSSION

In the previous sections, we have attempted fitting the observed continuum in the Prism spectrum of GN-z11 using combinations of an AGN or SF continuum model, a nebular continuum model, and Fe II emission models. In the SF case, the continuum excess originates from a Balmer continuum that has a temperature marginally higher than that derived from [O III] lines. In the AGN case, the continuum excess is better described by Fe II emission compared to a Balmer continuum. Purely based on the χ^2_ν, the best-fitting SF model and AGN model do not have significant differences. In this section, we discuss the implications of our results.

7.1 Presence of different ionized regions

7.1.1 Hot gas with hydrogen Balmer emission

As shown by Maiolino et al. (2024a), gas clouds with different densities are likely present in GN-z11. On the one hand, constraints from the semi-forbiddden N IV]λ1486 relative to [N IV]λ1483, and the relative strengths of the semiforbidden N III] multiplet indicate these UV emission lines to originate from high-density clouds with $n_{\rm H} \gtrsim 10^9$ cm^{-3}, consistent with BLR clouds On the other hand, the presence of strong, forbidden [O III]λ4363 requires densities much lower than the UV-line-emitting clouds, and consistent with NLR (or simple ISM) clouds.

In the SF case, the hydrogen-emitting clouds might be marginally hotter than the [O III]-emitting clouds and they could still come from the same spatial region. In the AGN case, we have shown, given the observed strength of Hγ, if the Balmer-line-emitting gas has a temperature similar to the [O III]-line-emitting gas, $T_e({\rm O}^{2+}) = 1.36 \pm 0.13 \times 10^4$ K, one expects a detectable Balmer jump clearly different from the shape of the continuum excess. If the continuum excess is dominated by some other mechanisms, which is our preferred solution, then the Balmer jump is weak enough that the best-fitting temperature would be $T_e({\rm H}^+) \approx 3 \times 10^4$ K, implying the observed Balmer emission to originate from gas much hotter than the forbidden-line-emitting gas.

We note that low-redshift observations of individual H II regions or PNe frequently show $T_e({\rm H}^+) < T_e({\rm O}^{2+})$ (e.g. Peimbert 1967), clearly the opposite to what we found in GN-z11. In the low-redshift cases, the temperature difference potentially rises from microfluctuations of temperature or chemical abundance inhomogeneities within individual nebulae (Peimbert et al. 2017). In the case of GN-z11, however, we argue the temperature difference is created by the spatial distributions of gas clouds responsible for different emission lines.

In the AGN case, the observed Balmer emission can have two components, one from hot and dense gas close to the accretion disc (the BLR), and the other from less-dense and colder clouds at a larger distance from the accretion disc (the NLR or SF-ionized ISM). These two components are not separable kinematically due to the limited spectral resolution. The hot-dense component has a negligible Balmer jump due to its high temperature, and the Balmer jump in the cold and low-density component is weak simply because the flux of the cold component is subdominant. Forbidden lines such as [O III]λ4363 are only present in the cold and low-density gas, together with the cold Balmer component, due to their low critical densities. One might wonder whether this explanation leads to an unphysically high [O III]λ4363/Hγ in the cold gas. Interestingly, high [O III]λ4363/Hγ values have been observed in a number high-z galaxies by *JWST*, especially AGNs (Mazzolari et al. 2024; Übler et al. 2024), with a few galaxies even showing [O III]λ4363/H$\gamma \sim 1$. A hard ionizing radiation from AGN combined with metal-poor gas can give rise to a high [O III]λ4363/Hγ in an NLR. For a rough estimation, if we simply use [O III]λ4363/H$\gamma < 1$ to set a prior for the flux of the cold Hγ, and fit the continuum assuming both a hot and a cold component (whose temperature is fixed to 1.3×10^4 K), we obtain ${\rm H}\gamma_{\rm cold} = 0.43^{+0.24}_{-0.14}{\rm H}\gamma_{\rm total}$. This calculation also slightly lowers the temperature estimation for the hot component to $T_e = 2.6^{+0.4}_{-0.6} \times 10^4$ K.

We emphasize that for the hot component, a high density is necessary to explain the missing Balmer jump while avoiding overpredicting the strength of [O III]λ4363. This requirement rules out the possibility of the hot component being the ionized gas within the low-density NLR or the ISM ionized by young stars. In addition, for the ISM ionized by young stars, it is difficult to reach a temperature of $T_e \sim 3 \times 10^4$ K. One might wonder whether the BLR can reach such a high temperature. Indeed, due to the high density of the gas and the absence of dust depletion, the cooling through metals within the BLR could be efficient. However, cooling in the BLR would be limited to semiforbidden and permitted transitions due to the high density. With CLOUDY, we calculated volume-average electron temperatures in clouds ionized by young stellar populations and AGN, as shown in Fig. D1. While SF models cannot produce high enough temperatures even if $\log(Z/{\rm Z}_\odot) \sim -3$, both NLR and BLR models are able to reach $T_e({\rm H}^+) \sim 3 \times 10^4$ K at $\log(Z/{\rm Z}_\odot) \sim -1$ and $\log(U) \sim -1$. The problem with the NLR model, however, is that the corresponding [O III]λ4363 is too strong compared to what has been observed in GN-z11.

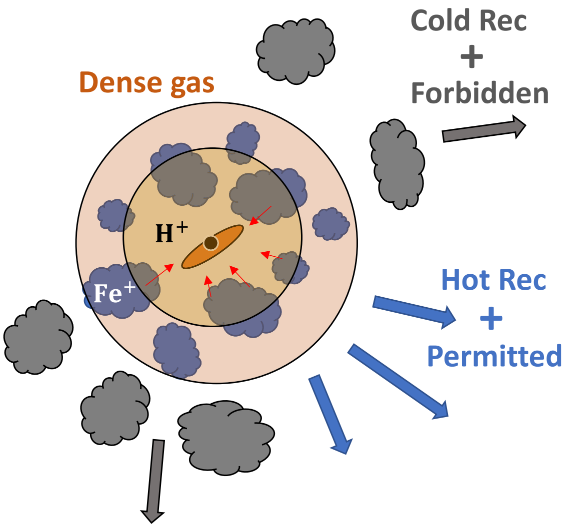

Figure 11. Schematic plot illustrating the inferred ionization structure within the nuclear region of GN-z11. In the central BLR that hosts dense gas clouds, Balmer recombination emission including continua and lines comes from the inner and hot region. In contrast, permitted emission of Fe II mainly comes from partially ionized region at large column densities, where the clouds might be infalling. Finally, outside the BLR and in the rest of the galaxy, there is also Balmer recombination emission from low-density gas with lower temperatures, which is cospatial with forbidden lines of metals. The plot does not reflect the actual physical scales of different regions.

Another complicating factor for BLRs is the physical conditions for different emission line specifies can well be different as they are optimally emitted by different clouds (Baldwin et al. 1995). Again, we caution that when the Balmer edge become partially optically thick in the BLR, it can be suppressed at the same level but at a lower temperature (Grandi 1982). Regardless, the requirement for the gas to be dense remains the same, and the presence of a BLR is preferred given the little contribution of the Balmer continuum to the small blue bump.

Fig. 11 shows our inferred ionization structure in the nuclear region of GN-z11. The BLR produces the continuum excess we see in the near-UV as well as permitted and semiforbidden emission lines. The Balmer continuum originates in a hot and dense region within the BLR. In contrast, Fe II emission likely originates in a partially ionized zone with high column densities. Finally, forbidden lines and part of the Balmer lines in the optical come from a less dense and colder region in the NLR or the ISM. Although we propose the Balmer lines to have origins from different regions, they are kinematically indistinguishable, especially with the limited S/N of current observations. Indeed, the broadening of lines in the BLR of GN-z11 by virial motions is only on the order of a few hundred kilometres per second due to its small black hole mass (Maiolino et al. 2024a). However, it may be possible to spatially resolve some of the NLR/ISM components with integral field spectroscopy, as illustrated in Maiolino et al. (2024b).

The presence of two Balmer components would also indicate biases in abundance estimations based on the assumption that the entire Balmer emission comes from the forbidden-line-emitting clouds. Our estimated $\mathrm{H}\gamma_{\mathrm{cold}}$ corresponds to $[\mathrm{O\,III}]\lambda4363/\mathrm{H}\gamma_{\mathrm{cold}} \approx 0.53^{+0.33}_{-0.09}$, resulting in an abundance of $12 + \log(\mathrm{O/H}) = 8.18^{+0.48}_{-0.27}$ assuming higher ionization states of oxygen are negligible. The uncertainties in the above value include uncertainties in the flux of $\mathrm{H}\gamma_{\mathrm{cold}}$ as well as uncertainties in the O^{2+} temperature. Although there is another uncertainty associated with converting the O^{2+} temperature to the O^{+} temperature in the NLR, it is at the level of ~ 0.01 dex in our case assuming the temperature relations for AGNs in Dors et al. (2020). While our lower abundance estimation is broadly consistent with the value obtained by Cameron et al. (2023a), the fiducial value we obtained is about 30 per cent of the solar value and is about two times the previously estimated value. High chemical abundances in high-z AGNs are commonly seen (Nagao, Marconi & Maiolino 2006a, b; Juarez et al. 2009; Matsuoka et al. 2009, 2011, 2018; Guo et al. 2020). We caution, however, that the range of the abundance we derived depends on the prior on the range of $[\mathrm{O\,III}]\lambda4363/\mathrm{H}\gamma_{\mathrm{cold}}$. A lowered upper limit for $[\mathrm{O\,III}]\lambda4363/\mathrm{H}\gamma_{\mathrm{cold}}$ would produce an overall lower metallicity estimation. To settle this problem, it is vital to have high spectral resolution observations of Balmer lines, which are unfortunately missed due to the truncation of the high-resolution NIRSpec grating spectrum in the previous observation (Maiolino et al. 2024a).

7.1.2 *Infalling gas with a high column density*

As we show in the previous section, under the AGN-dominated assumption, if Fe II emission is responsible for the observed bump in GN-z11, the gas with Fe II emission should be redshifted at a velocity of $\sim 3000\ \mathrm{km\,s^{-1}}$ with respect to other line-emitting regions. Such a high velocity would indicate a fast inflow. As shown by Hu et al. (2008a, b), it is not uncommon for Fe II emission to be redshifted with respect to narrow and broad emission lines in quasars. Within a sample of 4037 quasars from SDSS (York et al. 2000) at $z < 0.8$ inspected by Hu et al. (2008b), the typical velocity shift of Fe II is $\sim 400\ \mathrm{km\,s^{-1}}$, and the largest velocity shift of Fe II clearly exceeds $2000\ \mathrm{km\,s^{-1}}$ and even reaches $3000\ \mathrm{km\,s^{-1}}$.

To explain the ubiquitous shift in Fe II velocity, Ferland et al. (2009) proposed a scenario where Fe II emission comes from infalling clouds with large column densities viewed from their shielded faces, to which the gravitational pull overcomes radiation pressure from accreting supermassive black holes (SMBHs). In fact, for the SMBH in GN-z11 that is likely accreting at a super-Eddington rate of $L/L_{\mathrm{Edd}} \sim 5$ (Maiolino et al. 2024a), the required column density would be $7.5 \times 10^{24}\ \mathrm{cm^{-2}}$ according to the equation given by Ferland et al. (2009). The column density needed is in good agreement with the best-fitting Fe II model we adopted.

Finally, the infalling Fe II-emitting clouds should have a high Fe abundance as well to enhance the Fe II emission at $3000\ \text{Å} < \lambda < 3550\ \text{Å}$. An interesting question is whether the potentially enriched Fe is related to the 'abundance anomaly' in GN-z11, where nitrogen appears particularly enriched compared to oxygen, which we discuss in the next subsection.

7.2 Revisiting the 'abundance anomaly'

One of the most puzzling features in the spectrum of GN-z11 is the strong N IV] and N III] emission in the UV. Based on the high N III]/O III] in the UV, Bunker et al. (2023) and Cameron et al. (2023a) derived a supersolar N/O, indicating a fast and/or exotic chemical enrichment in GN-z11. With the new evidence from the potential Fe II emission, it is possible that iron is also enriched in GN-z11. It is noteworthy that high Fe abundances were also found in nitrogen-loud quasars at lower redshifts and were predicted by chemical enrichment models of quasars (e.g. Hamann & Ferland 1993). In addition, recent *JWST* observations have revealed potential early enrichment of Fe as traced by forbidden transitions of Fe in a galaxy showing a prominent Balmer jump at $z = 5.94$ (Cameron et al. 2024; Tacchella et al. 2025), and in an AGN host galaxy at $z = 5.55$ (Übler et al. 2023; Ji et al. 2024). To explain the high N/O, Maiolino et al. (2024a) suggest a possibility that the UV emission mainly originates in the BLR of the AGN in GN-z11, making the fast chemical enrichment within such a small region ($\sim 10^{-2}$ pc) and small gas mass (a few solar masses) possible without invoking any exotic enrichment channels. Similarly, since the Fe II emission mainly comes from clouds in the BLR, a fast enrichment of Fe towards the solar value is also compatible with the scenario above.

In addition to the fast enrichment of the overall chemical abundances within a small region, it is possible to achieve high Fe/O at low metallicities, which would give rise to the a strong Fe II complex without invoking a high oxygen abundance. According to the models of Vanni et al. (2023), it is possible for high-mass pair-instability supernovae (PISNe) to produce supersolar Fe/O even when Fe/H is as low as 1–10 per cent the solar value. An early enrichment of Fe is also possible through ejecta from hypernovae (HNe), especially given a potentially dense star formation environment of GN-z11 (Isobe et al. 2023; Watanabe et al. 2024). It is noteworthy that solar abundance ratios of Fe/O have also been observed in several extremely metal-poor galaxies in the local Universe and it is suspected that the enrichment of Fe is produced by PISNe, HNe, or SNe of supermassive stars with stellar masses of $M_* \gtrsim 300\ \mathrm{M}_\odot$ (e.g. Kojima et al. 2021; Isobe et al. 2022). The production of supermassive stars, on the other hand, might come from the stellar encounters in the dense nuclear environment of GN-z11 as suggested previously for dense globular clusters (Gieles et al. 2018). In the local Universe, Fe is mainly enriched by Type-Ia SNe that has a typical delay time from 100 Myr to 1 Gyr. However, we note that the first Type-Ia SNe can occur only ~ 30 Myr after the initial star formation (see e.g. Maiolino & Mannucci 2019, and references therein). According to the SED fitting of the *JWST*/NIRCam photometry of GN-z11 by Tacchella et al. (2023b), the extended part of the source has an SFH with a rising SFR starting from a lookback time of ~ 50 Myr, which then shows a peak of SFR at a lookback time of ~ 20 Myr. Therefore, it is still possible that the initial enrichment of Fe by Type-Ia SNe from the progenitors created in the rising phase of the past star formation starts to take effect at the time of observation. However, such a scenario would also require suppression of oxygen enrichment by previous core-collapse supernovae (CCSNe), or a dilution of the oxygen abundance, which might be achieved through inflow of pristine gas. Still, considering the mismatch between our photoionization models and data due to gaps in the models, it is important for future work to have more detailed modelling of the emission lines in the BLR in the early Universe.

Finally, a caveat of interpreting the strong high-ionization UV lines in GN-z11 as a sign of a high abundance is the optical-depth effect in BLRs. As the density and ionization parameter in an BLR become too high, the emission lines start to be dominated by a blackbody component near the surface of the cloud and their ratios no longer reflect the actual chemical abundances (Temple et al. 2021). To check this effect, we computed a series of photoionization models for BLRs having a range of hydrogen densities and ionization parameters while adopting a low metallicity and N/O. We found at $\log(Z/Z_{\odot}) = -1$ and $\log(\mathrm{N/O}) = -1.5$, both N III]/O III] and N IV]/O III] can be greater than one when $\log(U)$ reaches 0 and the surface emission starts to dominate. However, at such a high ionization parameter, N IV] would be significantly stronger than N III], which contradicts the similar fluxes of N IV] and N III] observed in GN-z11. Therefore, with a BLR origin for the UV nitrogen lines, we still need chemically enriched gas in order to match models with the observation.

7.3 Potential implications of the Bowen emission

While in the previous section, we fitted the emission feature detected at $\sim 3\sigma$ at 3133 Å with a redshifted peak within the UV Fe II complex, it is also possible that the emission feature is the Bowen fluoresence line, O IIIλ3133. This line is produced via fluorescence of O IIIλ303.8 with He II Lyα (i.e. Bowen fluorescence; Bowen 1934), and it is usually the strongest Bowen line of O III in the near UV. Strong O IIIλ3133 emission has been observed in AGNs, PNe, symbiotic stars (Kastner & Bhatia 1996), and more recently, in a galaxy at $z = 12.34$ (Castellano et al. 2024).

The strength of O IIIλ3133 strongly depends on the fraction of He II Lyα photons that are resonantly absorbed by O IIIλ303.8 and converted to Bowen emission, or the 'Bowen efficiency' (Kallman & McCray 1980). Thus, the flux of the Bowen line is sensitive to the shape of the ionizing SED as well as the metallicity, which greatly impacts the resulting abundance ratio of $\mathrm{He}^{++}/\mathrm{O}^{++}$ in the ionized gas. The physical conditions of the BLR in GN-z11 could provide the environment that boosts the strength of the Bowen emission. According to the photoionization calculations by Netzer, Elitzur & Ferland (1985), in dense PNe or BLRs of AGNs, the flux of O IIIλ3133 can be similar or even several times higher than that of He IIλ4686. While the *JWST* spectra of GN-z11 do not cover He IIλ4686, we can use the flux of He IIλ1640 to make a rough estimation. This is motivated by the fact that the flux ratio of He IIλ1640/He IIλ4686 is typically $7-8$ in all kinds of nebulae. According to the measurements by Maiolino et al. (2024a), $F(\mathrm{HeII}\lambda1640) = 6.0^{+1.4}_{-1.3} \times 10^{-19}$ erg s cm^{-2}. Our measured flux of the emission line at 3133 Å is $8.5 \pm 2.7 \times 10^{-20}$ erg s^{-1} cm^{-2}, which is roughly 1/7 of the flux of He IIλ1640. Therefore, the strength of the Bowen emission line is likely similar to that of He IIλ4686 and is indeed what one would expect for a BLR origin.

To better understand the origin of this line, it is important to reexamine *JWST*-confirmed high-z Type-1 AGNs with strong He IIλ4686 emission. Also, it would be useful to compute photoionization models with physical conditions appropriate for AGNs in early galaxies. However, this is beyond the scope of the current paper, and we leave it for future investigations.

7.4 Is the small blue bump unique?

In previous sections, we discussed potential physical origins for the small blue bump in GN-z11. Specifically, we investigated the scenarios where the bump is part of a Balmer continuum or a blend of Fe II lines. One might wonder whether there is other observational evidence of similar bumps in the spectra of early galaxies. Given the extreme physical conditions of GN-z11, it is possible that the small blue bump is a rare case. Interestingly, we did find another galaxy in JADES that show a very similar continuum excess in the UV. This galaxy, JADES-GS + 53.11243-27.77461, has a redshift of 9.433 and was observed in the GOODS South field (hereafter JADES-GS-z9-0) in both Cycle 1 Program 1210 (PI: N. Luetzgendorf; Bunker et al. 2024) and Cycle 2 Program 3215 (PI: D. Eisenstein; Eisenstein et al. 2023b). Its nebular emission was analysd by Cameron et al. (2023b), and it was later classified as a Type-2 AGN by Scholtz et al. (2025) based on UV emission-line diagnostics and the presence of the high ionization line [Ne IV]λ2422 (as well as the absence of broad emission lines), and more recently by Curti et al. (2025) based on the detection of the coronal line [Ne V]λ3426.

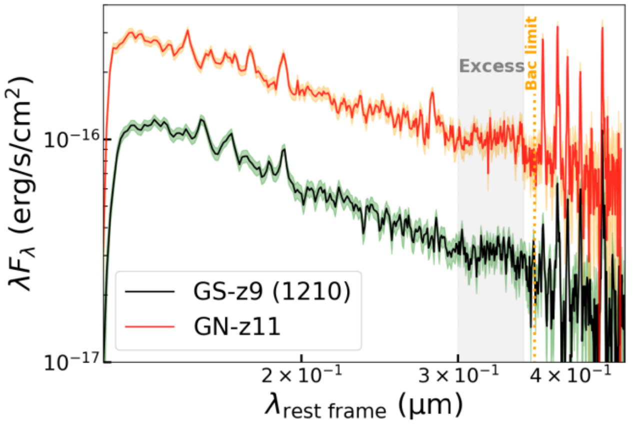

Figure 12. Comparison between the Prism spectrum of JADES-GS-z9-0 and that of GN-z11 on a log scale. The shaded regions correspond to the 1σ uncertainties of the spectra. The grey band marks the continuum excess region and the orange dotted line marks the location of the Balmer limit.

Fig. 12 shows the Prism spectrum of JADES-GS-z9-0 from the Program 1210 along with the Prism spectrum of GN-z11. One can see a bump within the continuum excess region in JADES-GS-z9-0, whose shape, however, is different from that in GN-z11 and does not exhibit a sharp jump at $\sim$ 3550. While the bump in JADES-GS-z9-0 cannot be well described by a Balmer continuum, Fe II models cannot provide a good fit as well due to the smoothly declining edge of the bump.

Intriguingly, the small blue bump in JADES-GS-z9-0 disappears in the observation of the Program 3215. Fig. 13 shows a comparison between the Prism spectrum in the Program 1210 and that in the Program 3215 for JADES-GS-z9-0. While the overall UV continuum rises in 3215 (as shown by the overall positive residuals), the UV slope slightly flattens. By fitting power-law functions to the UV continua of the two spectra, we obtained a slope of $\beta = -2.47 \pm 0.04$ for the 3215 spectrum when including the Balmer continuum, and $\beta = -2.35 \pm 0.03$ when excluding the Balmer continuum. In comparison, the UV slope of the 1210 spectrum is $\beta = -2.58 \pm 0.03$ if the bump region is excluded. We checked the shutter positions of the two observations and found the positioning is unlikely the cause to the difference of the UV flux. Also, the two Prism spectra were obtained with the same data reduction procedure.

In the rest frame of JADES-GS-z9-0, the two observations are separated by $\sim$ 1 month and we speculate this systematic change in the UV is indicative of spectral variability in the AGN. While JADES-GS-z9-0 was a Type-2 AGN classified from the previous observations, we might be witnessing the rise of of the underlying UV continuum from the AGN accretion disc, a process found in 'changing-look quasars' in lower redshifts (MacLeod et al. 2019). The small blue bump either has responded to the change of the UV continuum in 3215, or is simply overwhelmed by the rising continuum. According to the standard BLR model with a stratified ionization structure, emission from different ionic species respond to

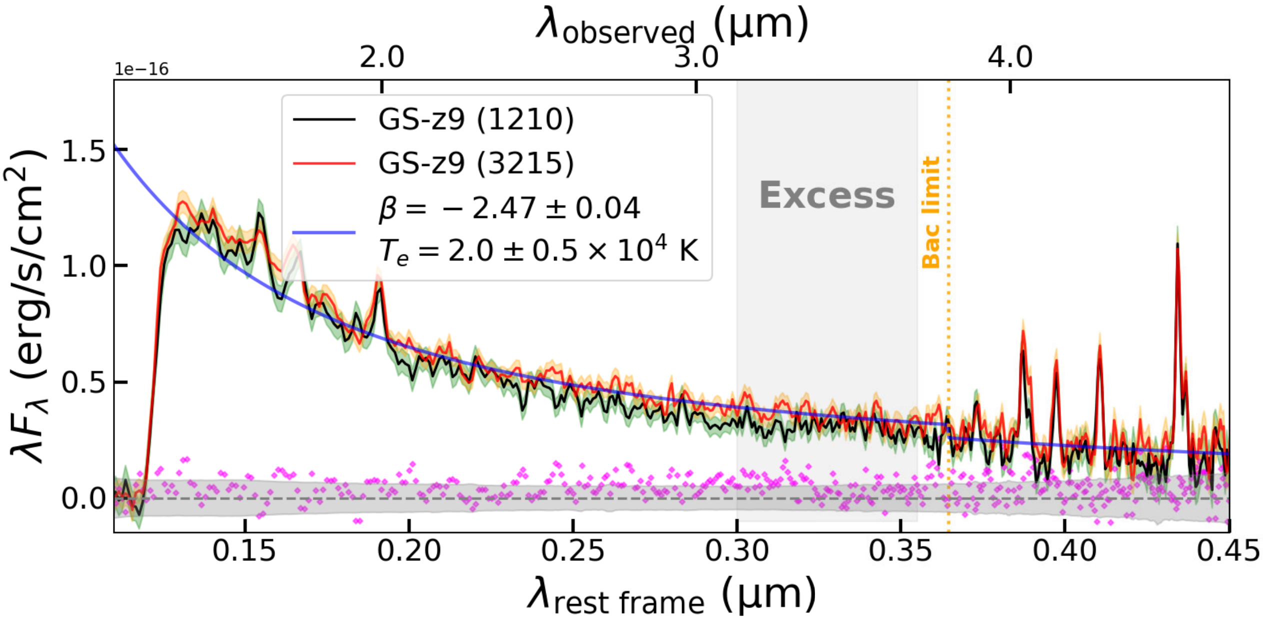

Figure 13. NIRSpec/Prism spectra of JADES-GS-z9-0 from the Cycle 1 Program 1210 and the Cycle 2 Program 3215. The two observations are separated by $\sim$ 1 month in the rest frame of JADES-GS-z9-0. The shaded regions represent 1σ uncertainties of the spectra. The magenta diamonds are the differences between the fluxes the two spectra. The horizontal grey shaded band indicates the 1σ uncertainty of the spectral difference. The blue line is a fit to the continuum of the JADES-GS-z9-0 in 3215 using a power-law function and an optically thin Balmer continuum model. The vertical grey shaded band indicates the continuum excess region in 1210. The orange dotted line indicates the location of the Balmer limit at 3646 Å.

the continuum variability differently (Ulrich et al. 1997). Therefore, the variability of the small blue bump could provide clues on its origin, which requires follow-up observations of this target. In fact, the UV continuum of JADES-GS-z9-0 in 3215 appears more smooth and can be described by a power-law function and an optically thin Balmer continuum with $T_e = 2.0 \pm 0.5 \times 10^4$ K, as shown in Fig. 13. The best-fitting Balmer temperature is consistent with the temperature inferred from [O III]λ4363 as well as the temperature inferred from O III]λ1666 (Curti et al. 2025).

In summary, the Prism spectrum JADES-GS-z9-0 shows a small blue bump at a similar spectral location as that in GN-z11, although with a slightly different shape. The bump in JADES-GS-z9-0 seems to be linked to its potential spectral variability. Future observations of the UV spectrum of JADES-GS-z9-0 is needed to verify the variability and provide more evidence on the identify of the small blue bump.

8 CONCLUSIONS

In this work, we investigated the physical origin of the continuum excess between 3000 and 3550 Å in the *JWST*/NIRSpec Prism spectrum of GN-z11. The continuum excess is significantly detected in the spectrum at 7.8σ and shows a sharp jump around 3550 Å. This excess in the UV partly resembles the shape of the small blue bump observed in typical quasar spectra, typically associated with Fe II complex emission from the BLR in the vicinity of the accreting SMBH. We investigated the origin of the continuum excess by fitting the observed spectrum with a combination of AGN/SF continuum models, nebular continuum models, and Fe II emission models. We summarize our findings in the following.

(i) If the UV continuum of GN-z11 is dominated by a stellar continuum, the continuum excess can be fitted by a Balmer continuum with a temperature of $T_e = 1.78^{+0.25}_{-0.21} \times 10^4$ K, which is marginally higher than the temperature derived from the optical [O III] lines of $T_e = 1.36 \pm 0.13 \times 10^4$ K.

(ii) If the UV continuum of GN-z11 is dominated by AGN continuum emission, a Balmer continuum alone cannot fit the continuum excess due to the significantly blueshifted jump of the continuum excess with respect to the Balmer limit. This indicates that the continuum excess in GN-z11 is not dominated by the Balmer continuum and that the Balmer continuum, if exists, is intrinsically weak.

(iii) The weakness of the Balmer continuum in the AGN case implies part of the Balmer emission should be associated with hot gas at a temperature of $T_e = 2.6^{+0.4}_{-0.6} \times 10^4$ K, which is much higher than the temperature traced by forbidden lines. Hence, the Balmer emission likely originates in the dense and hot part of the BLR, while forbidden lines are from the less dense and cool NLR or ISM. We note that, due to the small black hole mass in GN-z11, it is difficult to kinematically distinguish the two components in integrated spectra, as they have similar widths, but they may be separated in spatially resolved spectroscopy.

(iv) While the Fe II emission is typically stronger at $\lambda < 3000$ Å, we explored a series of CLOUDY models and found the Fe II emission at 3000 Å $< \lambda <$ 3550 Å can be significantly enhanced under certain conditions. Specifically, our fiducial models that show a prominent Fe II complex within the continuum excess region have $n_{\rm H} \sim 10^{11}$ cm^{-3}, $N_{\rm H} \sim 10^{25}$ cm^{-2}, $v_{\rm turb} \sim 300$ km s^{-1}, $\log(U) \sim -2.0$, and $\log(Z/Z_\odot) \gtrsim -0.5$ or [Fe/H] $\gtrsim -0.5$. These Fe II models show a prominent jump around 3500 Å, which can match the observed jump if the Fe II-emitting clouds are infalling at a velocity of $\sim$ 3000 km s^{-1}. Still, the Fe II models fail to reproduce the middle part of the jump due to the gaps in the models. Continuum/emission-line florescence not taken into accounted by current models might lead to this mismatch. Future modelling efforts focusing on the comparisons between models and observations between 3000 and 3550 Å are needed to fully solve this problem.

(v) The redshifted Fe II emission was also observed previously in low-redshift quasars, with the highest velocity shift reaching 3000 km s^{-1}. A potential explanation is that Fe II emission in BLRs is usually associated with infalling clouds with large column densities viewed from the shielded faces. The minimum column density required to drive the inflow is $\sim 7.5 \times 10^{24}$ cm^{-2}, consistent with the Fe II model we adopted and the likely Compton-thick nature of the BLR in GN-z11, and as inferred for several other AGN at high-z discovered by *JWST* (Maiolino et al. 2025).

(vi) The density of the Fe II models is consistent with the density inferred from high ionization lines, indicating their common origins in the BLR. On the other hand, the seemingly enriched Fe abundance could either be due to the fast enrichment of the overall chemical abundances within the small BLR, or result from a high Fe/O enriched by Type-Ia SNe or massive HNe/PISNe in the nuclear region.

(vii) We found a continuum bump at a similar spectral range in another AGN found in JADES, JADES-GS-z9-0. However, the continuum excess in JADES-GS-z9-0 has a slightly different shape. Interestingly, the UV spectrum of JADES-GS-z9-0 shows variability between observations at two different epochs, with the continuum excess disappear under the rising continuum at the later epoch. We speculate the varying continuum is driven by a changing-look AGN. Whether and how the continuum excess responds to the continuum variability could provide further clues on its origin. It is thus important to have follow-up monitoring of the target to verify the variability as well as characterizing its pattern.

We conclude by emphasizing that the presence of this small blue bump in GN-z11 and its peculiar properties demonstrates the need to re-examine previous theoretical models over a less frequently explored spectral regime, using typically subdominant spectral features in lower redshifts, and in an entirely new parameter space. In the meantime, new observational evidence from higher S/N spectra, especially at high spectral resolution and high spatial resolution with the IFU (e.g. $R \sim 2700$ IFU spectroscopy with NIRSpec), are needed to verify the current interpretations on GN-z11, especially the presence of distinct ionized regions and its exotic chemical abundance pattern in the very early Universe.

ACKNOWLEDGEMENTS

We thank the anonymous referee, whose thoughtful comments and suggestions improved the clarity of this work. XJ, RM, FDE, JS, and JW acknowledge ERC Advanced Grant 695671 ‘QUENCH’ and support by the Science and Technology Facilities Council (STFC) and by the UKRI Frontier Research grant RISEandFALL. RM acknowledges funding from a research professorship from the Royal Society. JC acknowledges funding from the ‘FirstGalaxies’ Advanced Grant from the European Research Council (ERC) under the European Union’s Horizon 2020 research and innovation programme (grant agreement no. 789056). ECL acknowledges support of an STFC Webb Fellowship (ST/W001438/1). BER acknowledges support from the NIRCam Science Team contract to the University of Arizona, NAS5-02015, and JWST Program 3215. BRP acknowledges support from the research project PID2021-127718NB-I00 of the Spanish Ministry of Science and Innovation/State Agency of Research (MICIN/AEI/10.13039/501100011033). ST acknowledges support by the Royal Society Research Grant G125142. The research of CCW is supported by NOIRLab, which is managed by the Association of Universities for Research in Astronomy (AURA) under a cooperative agreement with the National Science Foundation.

DATA AVAILABILITY

The *JWST*/NIRSpec data used in this paper are available through the MAST portal. The reduced Prism spectrum of GN-z11 we used for our main analyses can be accessed using this link. The reduced Prism spectra for individual observations of GN-z11 listed in Table 1 are available from the JADES DR3. All analysis results of this paper will be shared on reasonable request to the corresponding author.

REFERENCES

Abbott D. C., Conti P. S., 1987, ARA&A, 25, 113
Álvarez-Márquez J. et al., 2025, A&A, 695, A250
Alves de Oliveira C. et al., 2018, in Peck Alison B., eds, Observatory Operations: Strategies, Processes, and Systems VII. SPIE - International Society for Optics and Photonics, Austin, Texas, USAp. 107040Q, preprint (arXiv:1805.06922)
Baldwin J. A., Ferland G. J., Korista K. T., Hamann F., LaCluyzé A., 2004, ApJ, 615, 610
Baldwin J., Ferland G., Korista K., Verner D., 1995, ApJ, 455, L119
Berg D. A., Pogge R. W., Skillman E. D., Croxall K. V., Moustakas J., Rogers N. S. J., Sun J., 2020, ApJ, 893, 96
Bernini-Peron M. et al., 2024, A&A, 692, A89
Bevington P. R., Robinson D. K., 2003, Data Reduction and Error Analysis for the Physical Sciences. McGraw-Hill Education, Boston
Böker T. et al., 2023, PASP, 135, 038001
Bottorff M., Ferland G., Baldwin J., Korista K., 2000, ApJ, 542, 644
Bowen I. S., 1934, PASP, 46, 146
Brightman M., Ueda Y., 2012, MNRAS, 423, 702
Bunker A. J. et al., 2023, A&A, 677, A88
Bunker A. J. et al., 2024, A&A, 690, A288
Byler N., Dalcanton J. J., Conroy C., Johnson B. D., 2017, ApJ, 840, 44
Byrne C. M., Stanway E. R., Eldridge J. J., McSwiney L., Townsend O. T., 2022, MNRAS, 512, 5329
Cameron A. J. et al., 2023b, A&A, 677, A115
Cameron A. J., Katz H., Rey M. P., Saxena A., 2023a, MNRAS, 523, 3516
Cameron A. J., Katz H., Witten C., Saxena A., Laporte N., Bunker A. J., 2024, MNRAS, 534, 523
Cappellari M., 2017, MNRAS, 466, 798
Cappellari M., Emsellem E., 2004, PASP, 116, 138
Castellano M. et al., 2024, ApJ, 972, 143
Charbonnel C., Schaerer D., Prantzos N., Ramírez-Galeano L., Fragos T., Kuruvanthodi A., Marques-Chaves R., Gieles M., 2023, A&A, 673, L7
Conti P. S., Massey P., 1989, ApJ, 337, 251
Curti M. et al., 2023, MNRAS, 518, 425
Curti M. et al., 2024, A&A, 684, A75
Curti M. et al., 2025, A&A, 697, A89
Curtis-Lake E. et al., 2023, Nat. Astron., 7, 622
D’Eugenio F. et al., 2025, ApJS, 277, 4
de Graaff A. et al., 2024, A&A, 684, A87
Dietrich M., Hamann F., Appenzeller I., Vestergaard M., 2003, ApJ, 596, 817
Dorner B. et al., 2016, A&A, 592, A113
Dors O. L., Maiolino R., Cardaci M. V., Hägele G. F., Krabbe A. C., Pérez-Montero E., Armah M., 2020, MNRAS, 496, 3209
Draine B. T., 2011, Physics of the Interstellar and Intergalactic Medium. Princeton Univ. Press, Princeton, NJ
Eisenstein D. J. et al., 2023a, preprint (arXiv:2306.02465)
Eisenstein D. J. et al., 2023b, preprint (arXiv:2310.12340)
Feltre A., Charlot S., Gutkin J., 2016, MNRAS, 456, 3354
Ferland G. J. et al., 2017, Rev. Mex. Astron. Astrofis., 53, 385
Ferland G. J., Hu C., Wang J.-M., Baldwin J. A., Porter R. L., van Hoof P. A. M., Williams R. J. R., 2009, ApJ, 707, L82
Ferruit P. et al., 2022, A&A, 661, A81

Foreman-Mackey D., Hogg D. W., Lang D., Goodman J., 2013, PASP, 125, 306
Furtak L. J. et al., 2024, Nature, 628, 57
Gardner J. P. et al., 2023, PASP, 135, 068001
Garmany C. D., Massey P., Conti P. S., 1984, ApJ, 278, 233
Gaskell C. M., 1980, The Observatory, 100, 148
Gaskell M., Thakur N., Tian B., Saravanan A., 2022, Astron. Nachr., 343, e210112
Gieles M. et al., 2018, MNRAS, 478, 2461
Goodrich R. W., 1989, ApJ, 342, 224
Grandi S. A., 1981, ApJ, 251, 451
Grandi S. A., 1982, ApJ, 255, 25
Greene J. E. et al., 2024, ApJ, 964, 39
Grevesse N., Asplund M., Sauval A. J., Scott P., 2010, Ap&SS, 328, 179
Grogin N. A. et al., 2011, ApJS, 197, 35
Gunawardhana M. L. P., Brinchmann J., Croom S., Bunker A., Bryant J., Oh S., 2025, preprint (arXiv:2504.12584)
Guo Y. et al., 2020, ApJ, 898, 26
Gutkin J., Charlot S., Bruzual G., 2016, MNRAS, 462, 1757
Hamann F., Ferland G., 1993, ApJ, 418, 11
Hu C., Wang J.-M., Ho L. C., Chen Y.-M., Bian W.-H., Xue S.-J., 2008a, ApJ, 683, L115
Hu C., Wang J.-M., Ho L. C., Chen Y.-M., Zhang H.-T., Bian W.-H., Xue S.-J., 2008b, ApJ, 687, 78
Isobe Y. et al., 2022, ApJ, 925, 111
Isobe Y. et al., 2023, ApJ, 959, 100
Jakobsen P. et al., 2022, A&A, 661, A80
Jenkins E. B., 2009, ApJ, 700, 1299
Ji X. et al., 2024, MNRAS, 535, 881
Juarez Y., Maiolino R., Mujica R., Pedani M., Marinoni S., Nagao T., Marconi A., Oliva E., 2009, A&A, 494, L25
Kallman T., McCray R., 1980, ApJ, 242, 615
Kass R. E., Raftery A. E., 1995, J. Am. Stat. Assoc., 90, 773
Kastner S. O., Bhatia A. K., 1996, MNRAS, 279, 1137
Katz H. et al., 2024, preprint (arXiv:2408.03189)
Kocevski D. D. et al., 2023, ApJ, 954, L4
Koekemoer A. M. et al., 2011, ApJS, 197, 36
Kojima T. et al., 2021, ApJ, 913, 22
Komossa S., 2008, in Revista Mexicana de Astronomia y Astrofisica Conference Series. p. 86, preprint (arXiv:0710.3326)
Kovačević J., Popović L. Č., Kollatschny W., 2014, Adv. Space Res., 54, 1347
Lai S., Onken C. A., Wolf C., Bian F., Fan X., 2024, MNRAS, 527, 3912
Lambrides E. et al., 2024, preprint (arXiv:2409.13047)
Lanzuisi G. et al., 2018, MNRAS, 480, 2578
Laseter I. H. et al., 2024, A&A, 681, A70
Leighly K. M., 1999, ApJS, 125, 317
Liddle A. R., 2007, MNRAS, 377, L74
Liu X. W., Luo S. G., Barlow M. J., Danziger I. J., Storey P. J., 2001, MNRAS, 327, 141
Luridiana V., Morisset C., Shaw R. A., 2015, A&A, 573, A42
MacLeod C. L. et al., 2019, ApJ, 874, 8
Maiolino R. et al., 2024a, Nature, 627, 59
Maiolino R. et al., 2024b, A&A, 687, A67
Maiolino R. et al., 2024c, A&A, 691, A145
Maiolino R. et al., 2025, MNRAS, 538, 1921
Maiolino R., Mannucci F., 2019, A&AR, 27, 3
Malkan M. A., Sargent W. L. W., 1982, ApJ, 254, 22
Matsuoka K., Nagao T., Maiolino R., Marconi A., Taniguchi Y., 2009, A&A, 503, 721
Matsuoka K., Nagao T., Marconi A., Maiolino R., Mannucci F., Cresci G., Terao K., Ikeda H., 2018, A&A, 616, L4
Matsuoka K., Nagao T., Marconi A., Maiolino R., Taniguchi Y., 2011, A&A, 527, A100
Matthee J. et al., 2024, ApJ, 963, 129
Mazzolari G. et al., 2024, A&A, 691, A345
Mejía-Restrepo J. E., Trakhtenbrot B., Lira P., Netzer H., Capellupo D. M., 2016, MNRAS, 460, 187
Morisset C., Luridiana V., García-Rojas J., Gómez-Llanos V., Bautista M., Mendoza C., 2020, Atoms, 8, 66
Nagao T., Maiolino R., Marconi A., 2006b, A&A, 447, 863
Nagao T., Marconi A., Maiolino R., 2006a, A&A, 447, 157
Nakajima K. et al., 2018, A&A, 612, A94
Netzer H., Elitzur M., Ferland G. J., 1985, ApJ, 299, 752
Netzer H., Wills B. J., 1983, ApJ, 275, 445
Neugebauer G., Oke J. B., Becklin E. E., Matthews K., 1979, ApJ, 230, 79
Oesch P. A. et al., 2016, ApJ, 819, 129
Onoue M. et al., 2023, ApJ, 942, L17
Osterbrock D. E., Pogge R. W., 1985, ApJ, 297, 166
Peimbert M., 1967, ApJ, 150, 825
Peimbert M., Peimbert A., Delgado-Inglada G., 2017, PASP, 129, 082001
Penston M. V., 1987, MNRAS, 229, 1P
Pezzulli E., Valiante R., Orofino M. C., Schneider R., Gallerani S., Sbarrato T., 2017, MNRAS, 466, 2131
Richstone D. O., Schmidt M., 1980, ApJ, 235, 361
Rigby J. et al., 2023, PASP, 135, 048001
Roman-Duval J. et al., 2025, ApJ, 985, 109
Sanders R. L., Shapley A. E., Topping M. W., Reddy N. A., Brammer G. B., 2023, ApJ, 955, 54
Sanders R. L., Shapley A. E., Topping M. W., Reddy N. A., Brammer G. B., 2024, ApJ, 962, 24
Sarkar A. et al., 2021, ApJ, 907, 12
Schmidt G. D., Miller J. S., 1980, ApJ, 240, 759
Scholtz J. et al., 2024, A&A, 687, A283
Scholtz J. et al., 2025, A&A, 697, A175
Senchyna P., Plat A., Stark D. P., Rudie G. C., Berg D., Charlot S., James B. L., Mingozzi M., 2024, ApJ, 966, 92
Shields G. A., Ludwig R. R., Salviander S., 2010, ApJ, 721, 1835
Stanway E. R., Eldridge J. J., 2018, MNRAS, 479, 75
Tacchella S. et al., 2023a, MNRAS, 522, 6236
Tacchella S. et al., 2023b, ApJ, 952, 74
Tacchella S. et al., 2025, MNRAS, 540, 851
Temple M. J., Ferland G. J., Rankine A. L., Chatzikos M., Hewett P. C., 2021, MNRAS, 505, 3247
Topping M. W. et al., 2024, MNRAS, 529, 3301
Tsuzuki Y., Kawara K., Yoshii Y., Oyabu S., Tanabé T., Matsuoka Y., 2006, ApJ, 650, 57
Übler H. et al., 2023, A&A, 677, A145
Übler H. et al., 2024, MNRAS, 531, 355
Ulrich M. H. et al., 1980, MNRAS, 192, 561
Ulrich M.-H., Maraschi L., Urry C. M., 1997, ARA&A, 35, 445
Vanden Berk D. E. et al., 2001, AJ, 122, 549
Vanni I., Salvadori S., Skúladóttir Á., Rossi M., Koutsouridou I., 2023, MNRAS, 526, 2620
Verner E. M., Verner D. A., Korista K. T., Ferguson J. W., Hamann F., Ferland G. J., 1999, ApJS, 120, 101
Vernet J. et al., 2011, A&A, 536, A105
Véron-Cetty M. P., Véron P., Gonçalves A. C., 2001, A&A, 372, 730
Vestergaard M., Wilkes B. J., 2001, ApJS, 134, 1
Watanabe K. et al., 2024, ApJ, 962, 50
Wills B. J., Netzer H., Wills D., 1985, ApJ, 288, 94
Witstok J. et al., 2025, Nature, 639, 897
Witstok J., Smit R., Maiolino R., Curti M., Laporte N., Massey R., Richard J., Swinbank M., 2021, MNRAS, 508, 1686
Wu Q., Shen Y., 2022, ApJS, 263, 42
York D. G. et al., 2000, AJ, 120, 1579
Zamorani G. et al., 1981, ApJ, 245, 357

APPENDIX A: DETECTION OF THE SMALL BLUE BUMP IN JACKKNIFED PRISM SPECTRA

To check whether the small blue bump in the Prism spectrum of GN-z11 is caused by any detector artefact during observations, we Jackknifed the Prism spectra from independent measurements.

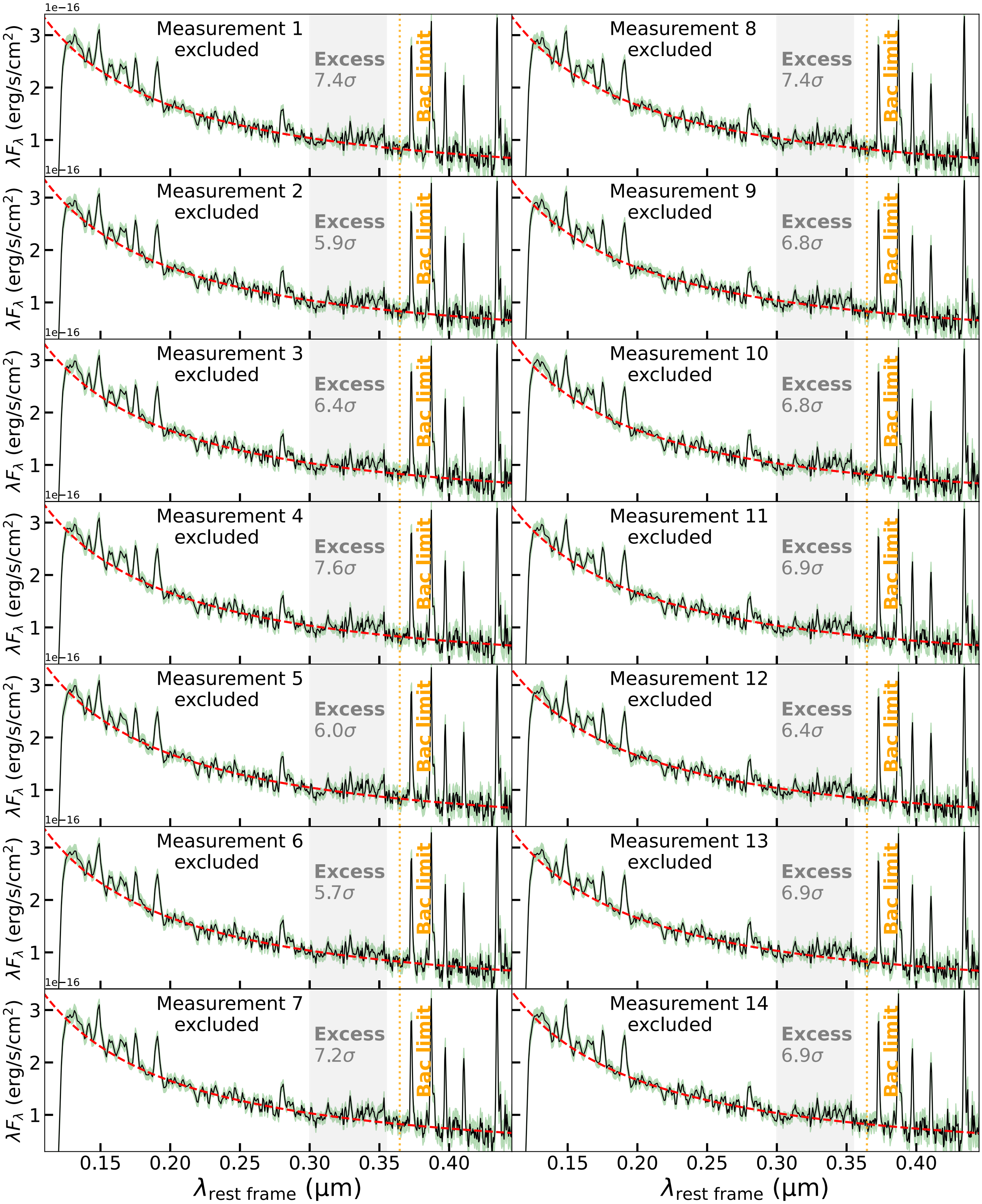

Figure A1. Jackknifed Prism spectra of GN-z11 generated from a total of 19 measurements. For each panel, one of the measurements is excluded and the rest of the measurements is combined via an inverse-variance weighted method with 3σ clipping. The green shaded regions indicate the combined 1σ uncertainties. In each panel, the dashed red line is the best-fitting power law for the continuum excluding the excess region. The grey shaded region marks the continuum excess region identified in the final spectrum combining all measurements. The significance of the integrated flux excess in the grey shaded region with respect to the power-law continuum is also shown. The orange dotted line marks the location of the Balmer continuum limit. The first 14 Jackknifed spectra are shown.

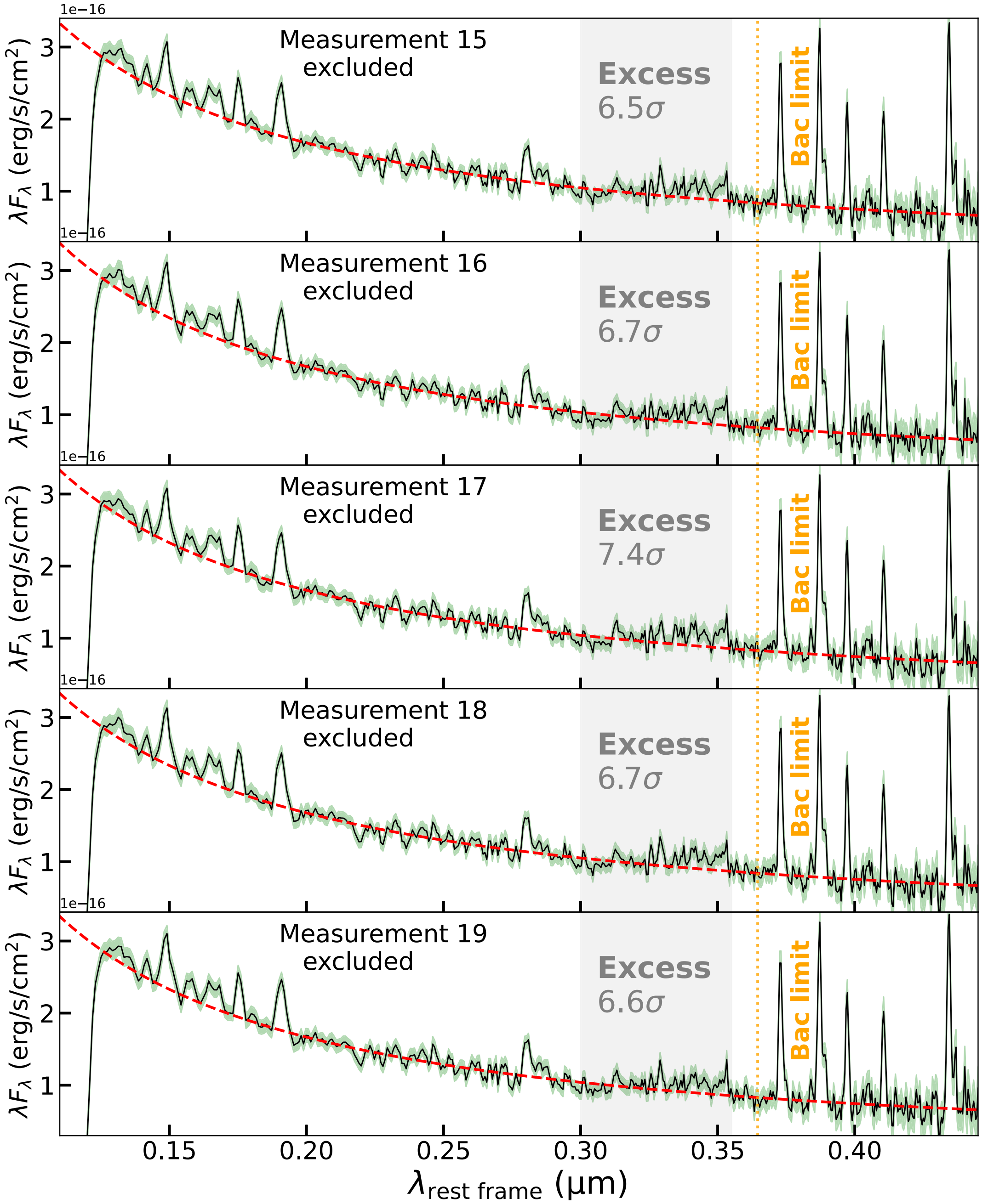

Figure A2. Jackknifed Prism spectra of GN-z11 generated from a total of 19 measurements. The remaining five Jackknifed spectra are shown.

The May observation of GN-z11 has seven unique MSA positions and a total of nine exposures. We considered exposures with the same shutter position as an independent trial, which results in seven trials for the May observation. Similarly, we identified 12 trials from a total of 24 exposures in February. In total, we have 19 measurements for Jackknifing.

Figs A1 and A2 show the 19 Jackknifed spectra from the measurements. Each spectrum was obtained by excluding one measurement and combining the rest of the measurements through inverse-variance weighting and 3σ clipping. It is clear that the continuum excess in the near-UV as well as the jump near 3550 Å persists in all Jackknifed spectra and is significant, confirming it is not an artefact driven by a single measurement. Meanwhile, the emission at 3133 Å is also visible in all the spectra. In contrast, a potential emission line at $\sim$ 3300 Å seemed disappeared when measurement 16 was excluded, meaning it is mainly from this measurement.

APPENDIX B: FITS WITH ALTERNATIVE CONTINUUM MODELS

B1 Power-law continuum model

In this appendix, we describe the fitting results by assuming the continuum of GN-z11 is a power law, without assuming any physical

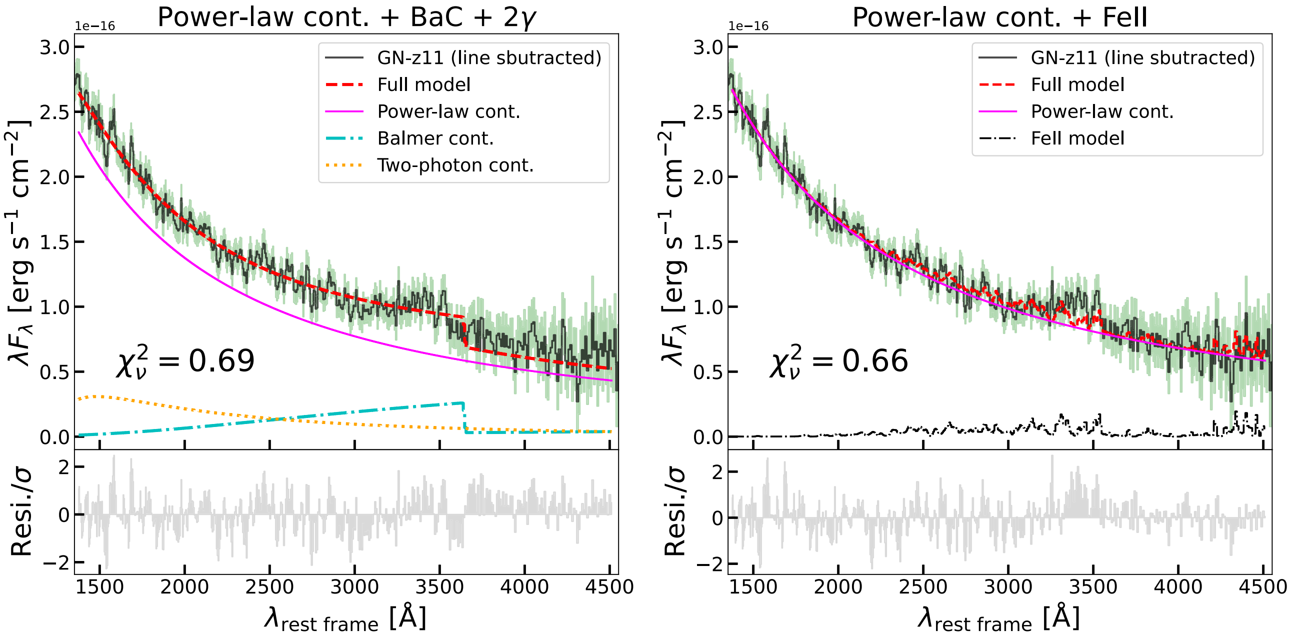

Figure B1. Best-fitting models for the line-subtracted Prism spectrum of GN-z11, where the continuum is assumed to be a power law. The top panels show the models with the reduced χ^2. The bottom panels show the χ residual of the fit. Left: fit combining a power-law continuum and nebular continuum. Right: fit combining a power-law continuum and Fe II emission. The fit involving Fe II produces a slightly smaller reduced χ^2.

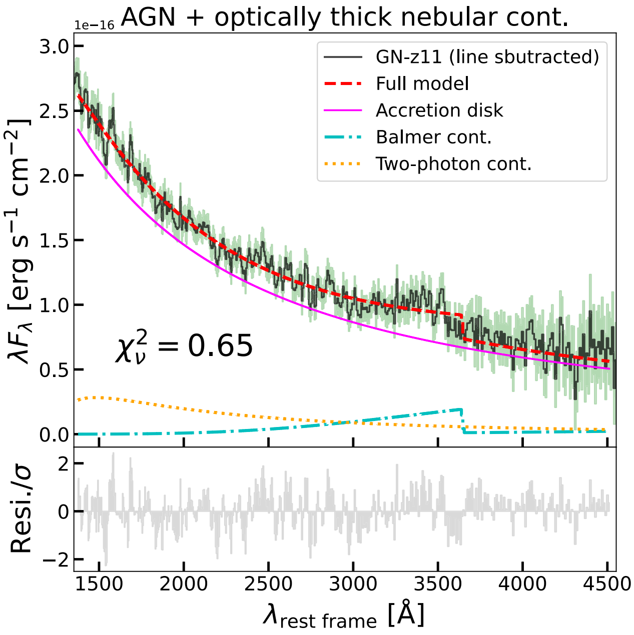

Figure B2. As Fig. 3, but where the Balmer continuum has been replaced by the partially optically thick case given by equation (B1). The top panel shows the best-fitting models. The bottom panel shows the χ residual of the fit.

origin as we did in the main text. Fig. B1 shows the fitting results from two models, where we used nebular continuum and Fe II emission to describe the continuum excess, respectively. The nebular continuum model and the Fe II model are described in Section 4. The fit using the nebular continuum model yields a best-fitting power-law slope of $\beta = -2.43 \pm 0.02$ and a best-fitting electron temperature of $T_e = 1.61^{+0.26}_{-0.20} \times 10^4$ K, close to the temperature estimate of the stellar-continuum fit ($T_e = 1.78^{+0.25}_{-0.21} \times 10^4$ K). The fit using the Fe II model yields a best-fitting power-law slope of $\beta = -2.28 \pm 0.02$. Overall, the reduced χ^2 is slightly smaller in the Fe II fit.

B2 Optically thick Balmer continuum model

In this appendix, we describe an attempt to fit the small blue bump by assuming a partially optically thick Balmer continuum, which includes an additional free parameter, the optical depth at the Balmer edge, τ_{BC}. This model was initially proposed by Grandi (1982) to describe line-emitting clouds that are heated towards large optical depths in quasars. Therefore, we considered the continuum to be dominated by an AGN SED from Pezzulli et al. (2017) in this case (see Section 4).

A partially optically thick Balmer continuum is increasingly suppressed at longer wavelengths due to the cubic dependence of the absorption cross-section on the wavelength. We adopted the functional form proposed by Grandi (1982)

$$F_{\lambda;\mathrm{thick}} = F_\lambda^{\mathrm{BE}} \frac{B_\lambda(T_e)(1 - e^{-\tau_\lambda})}{B_\lambda^{\mathrm{BE}}(T_e)(1 - e^{-\tau_{\mathrm{BE}}})}\ ;\ \lambda \leq \lambda_{\mathrm{BE}}, \tag{B1}$$

where F_λ^{BE} is the flux at the Balmer edge, $B_\lambda(T_e)$ is the *Planck* function, and $\tau_\lambda = \tau_{\mathrm{BE}}(\lambda/\lambda_{\mathrm{BE}})^3$ is the optical depth of the Balmer continuum at a given wavelength. The optically thick Balmer continuum is related to the optically thin one by

$$F_{\lambda;\mathrm{thick}} = F_{\lambda;\mathrm{thin}} \left(\frac{\lambda_{\mathrm{BE}}}{\lambda}\right)^3 \left[\frac{e^{-\tau_{\mathrm{BE}}} - e^{-(\tau_\lambda + \tau_{\mathrm{BE}})}}{1 - e^{-\tau_{\mathrm{BE}}}}\right], \tag{B2}$$

and it is reduced to the optically thin case when $\tau_{\mathrm{BE}} \to 0$. Fig. B2 shows the best-fitting model with $T_e = 8.2^{+1.2}_{-1.0} \times 10^3$ K and $\tau_{\mathrm{BE}} = 0.65^{+0.10}_{-0.09}$. The temperature is significantly lower than the forbidden-line temperature inferred from [O III]. If we interpret this as the optically thick Balmer continuum arising from dense BLR gas, the BLR gas needs to be colder than the low-density gas that

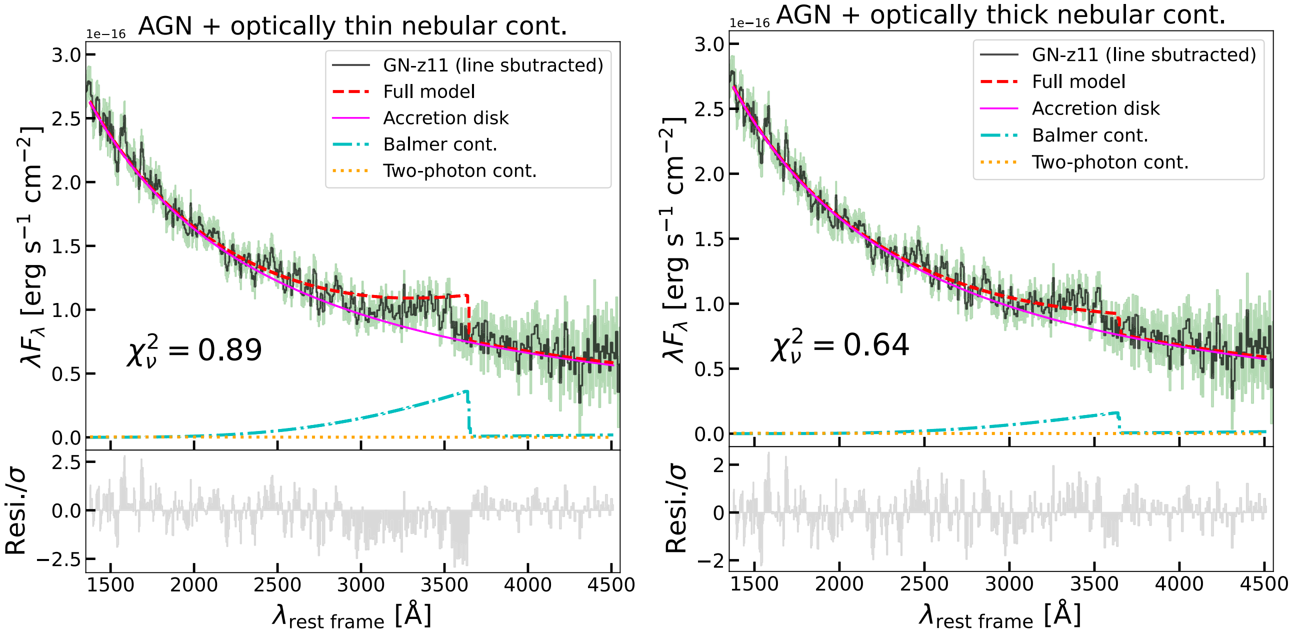

Figure B3. Best-fitting models for the line-subtracted Prism spectrum of GN-z11, where the two-photon continuum is suppressed due to the high density. The top panels show the models with the reduced χ^2. The bottom panels show the χ residual of the fit. Left: fit combining an AGN SED and optically thin nebular continuum. Right: fit combining an AGN SED and optically thick nebular continuum.

emits [O III]. However, from Appendix D, such a low temperature is implausible at a moderate ionization parameter of $\log(U) \gtrsim -3$ and a metallicity of $Z/Z_\odot \lesssim 1$. The reduced χ^2 of the fit is significantly smaller compared to the optically thin case shown in Fig. 3. Still, one caveat of this model is the treatment of the two-photon continuum. If the two-photon continuum has the same origin as the Balmer continuum (i.e. from the BLR), it should be significantly suppressed. It is also possible that the two-photon continuum comes from the low-density gas outside the BLR. In the latter case, however, the normalization of the two-photon continuum becomes uncertain. In the next appendix, we discuss fitting results with a suppressed two-photon continuum.

B3 High-density nebular continuum models

In this appendix, we present fitting results based on nebular continuum models assuming a high gas density of $n_{\rm H} = 10^6$ cm^{-3}, which strongly suppresses the two-photon continuum. The condition would be satisfied if the nebular continuum in GN-z11 predominantly comes from high-density gas, which is possible for the AGN scenario where there is a BLR component. Therefore, we investigate fits assuming an AGN-dominated continuum (see Section 4) specifically. Fig. B3 shows the fitting results for the optically thin and the optically thick nebular continuum case, respectively. In both models, it is clear that the two-photon continuum is strongly suppressed due to the high density. The optically thin model produces a worse fit compared to the case with a non-suppressed two-photon continuum as shown in Fig. 3 and has a lower best-fitting temperature of $\sim 7.5 \times 10^3$ K as reflected by the stronger jump. The optically thick model produces a much smaller reduced χ^2, although the best-fitting temperature is even lower, reaching $\sim 6.5 \times 10^3$ K, which is unlikely to be found in highly ionized gas as shown in Appendix D.

APPENDIX C: FE II JUMP IN QUASAR SPECTRA

In this appendix, we show a few more examples of quasar spectra that exhibit UV jumps blueward of the Balmer limit caused by Fe II emission. These quasars were selected from a sample of luminous quasars at $4.5 < z < 5.3$ in the XQz5 catalogue compiled by Lai et al. (2024). The spectra were obtained with X-shooter (Vernet et al. 2011) at the Very Large Telescope. These quasars have prominent UV continuum emission and their Eddington ratios are on average 0.3 dex higher than the lower redshift quasars in SDSS with similar black hole masses (Wu & Shen 2022; Lai et al. 2024).

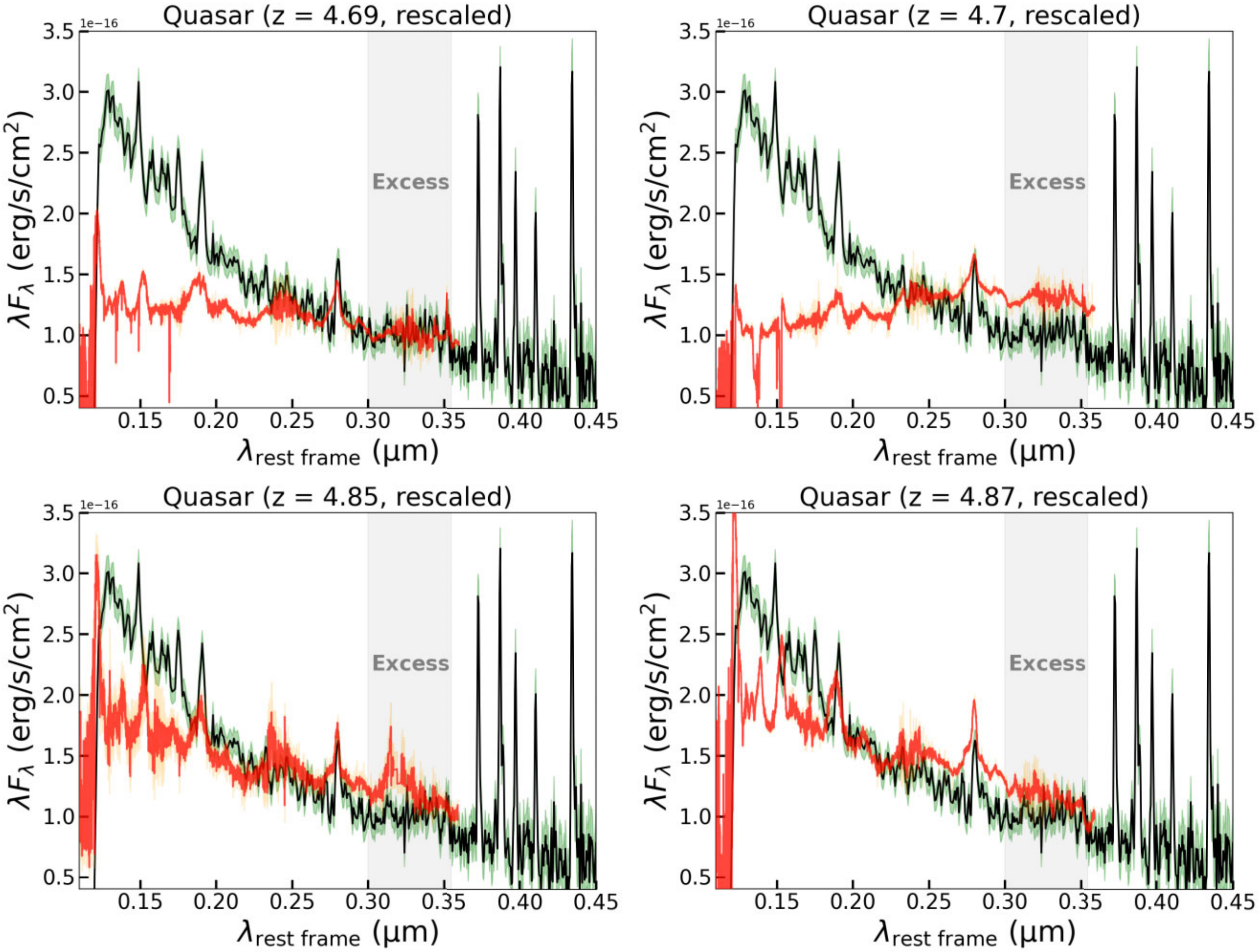

Figure C1. Comparison between the rest-frame UV spectra of quasars from Lai et al. (2024) and that of GN-z11. The quasar spectra are plotted as red solid lines with their 1σ uncertainties indicated by the orange shaded region. The fluxes of the quasars are rescaled. The spectrum of GN-z11 is shown as black solid lines in the back with the 1σ uncertainty indicated by the green shaded region. The continuum excess region we identified in GN-z11 is highlighted with the grey shaded band.

APPENDIX D: VOLUME-AVERAGE ELECTRON TEMPERATURES IN DIFFERENT IONIZED CLOUDS

Fig. D1 shows the CLOUDY predictions on the volume-average $T_e(\mathrm{H}^+)$ for clouds ionized by young stars and AGNs, respectively. For SF clouds, we adopted a fiducial model which uses the Binary Population and Spectral Synthesis models (BPASS; Stanway & Eldridge 2018; Byrne et al. 2022) assuming 1 Myr after a burst of star formation. Even with $\log(U) = -1$ and $\log(Z/\mathrm{Z}_\odot) = -3$, the volume-average $T_e(\mathrm{H}^+)$ is still lower than 3×10^4 K. In comparison, a low-density NLR can reach $T_e(\mathrm{H}^+) \sim 3 \times 10^4$ K at a fiducial metallicity of $\log(Z/\mathrm{Z}_\odot) = -0.84$ inferred for GN-z11 (Cameron et al. 2023a) and a $\log(U)$ between −1.5 and −1. At such a high temperature, however, the electron temperature traced by [O III]λ4363 in the NLR would be comparably high, which is inconsistent with what we observed in GN-z11.

Finally, for high-density BLR models, we calculate the volume-average temperature, $T_e(\mathrm{H}^+)$, within a column density of $N_\mathrm{H} = 10^{22}$ cm^{-3} at a fiducial density of $n_\mathrm{H} = 10^{11}$ cm^{-3}, which roughly encloses the H$^+$ zone for the range of ionization parameters we considered (Ferland et al. 2009). While the above parameters can produce $T_e(\mathrm{H}^+) \sim 3 \times 10^4$ K at $\log(Z/\mathrm{Z}_\odot) \sim -1$ and $\log(U) \sim -1$, it is possible for other combinations of n_H and N_H to achieve high temperatures.

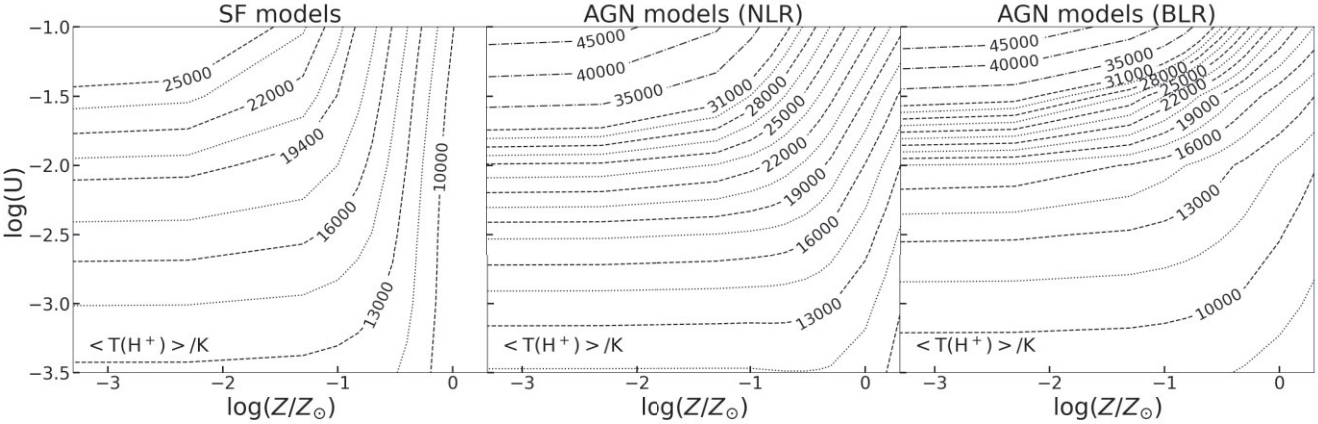

Figure D1. Predictions on hydrogen Balmer temperatures for clouds ionized by different sources as functions of the metallicity and ionization parameter. Left: contours of electron temperatures of SF models ionized by a simple stellar population from a 1 Myr-old starburst generated by BPASS assuming the default initial mass function with an upper mass limit of 300 $M_\odot$ described in Stanway & Eldridge (2018). Both the dashed and dotted lines are plotted with steps of 3000 K. Adjacent dashed and dotted lines are separated by 1500 K. Middle: contours of electron temperatures of NLR models ionized by an AGN SED the same as the one in Table 3. The hydrogen density of the models is set to 10^3 cm^{-3}. Right: contours of electron temperatures of BLR models ionized by an AGN SED the same as the one in Table 3. The hydrogen density of the models is set to 10^{11} cm^{-3} and the hydrogen column density is set to 10^{22} cm^{-2} as appropriate for the H$^+$ region within the BLR. While the SF models and NLR models include dust depletion, the BLR models do not.

This paper has been typeset from a TEX/LATEX file prepared by the author.